

# Scaling Relations for Dark Matter Annihilation and Decay Profiles in Dwarf Spheroidal Galaxies

Andrew B. Pace,<sup>1,2</sup> \* Louis E. Strigari<sup>1</sup>

<sup>1</sup>George P. and Cynthia Woods Mitchell Institute for Fundamental Physics and Astronomy, and Department of Physics and Astronomy, Texas A&M University, College Station, TX 77843, USA

<sup>2</sup> Mitchell Astronomy Fellow

Accepted XXX. Received YYY; in original form ZZZ

## ABSTRACT

Measuring the dark matter distribution in dwarf spheroidal galaxies (dSphs) from stellar kinematics is crucial for indirect dark matter searches, as these distributions set the fluxes for both dark matter annihilation (J-Factor) and decay (D-Factor). Here we produce a compilation of J and D-Factors for dSphs, including new calculations for several newly-discovered Milky Way (MW) satellites, for dSphs outside of the MW virial radius, and for M31 satellites. From this compilation we test for scaling relations between the J and D-factors and physical properties of the dSphs such as the velocity dispersion ( $\sigma_{\text{los}}$ ), the distance ( $d$ ), and the stellar half-light radius ( $r_{1/2}$ ). We find that the following scaling relation minimizes the residuals as compared to different functional dependencies on the observed dSphs properties  $J(0.5^\circ) = 10^{17.72} (\sigma_{\text{los}}/5 \text{ km s}^{-1})^4 (d/100 \text{ kpc})^{-2} (r_{1/2}/100 \text{ pc})^{-1}$ . We find this relation has considerably smaller scatter as compared to the simpler relations that scale only as  $1/d^2$ . We further explore scalings with luminosity ( $L_V$ ), and find that the data do not strongly prefer a scaling including  $L_V$  as compared to a pure  $1/d^2$  scaling. The scaling relations we derive can be used to estimate the J-Factor without the full dynamical analysis, and will be useful for estimating limits on particle dark matter properties from new systems that do not have high-quality stellar kinematics.

**Key words:** galaxies: kinematics and dynamics – cosmology: theory – dark matter

## 1 INTRODUCTION

Dwarf spheroidal galaxies (dSphs) have proven to be ideal targets for gamma-ray searches from particle dark matter annihilation or decay (Conrad et al. 2015). The Fermi-LAT combined limits from the dSphs with well-measured stellar kinematics place strong bounds on the dark matter annihilation cross section, with sensitivity to cosmologically-motivated models in the mass range  $\sim 10 - 100$  GeV (Abdo et al. 2010; Geringer-Sameth & Koushiappas 2011; Ackermann et al. 2011, 2014; Geringer-Sameth et al. 2015a; Ackermann et al. 2015). More massive dark matter particles,  $\sim 100$  GeV - 100 TeV, are now being probed by ground-based gamma-ray observatories (Abramowski et al. 2014; MAGIC Collaboration 2016; Albert et al. 2017a; Archambault et al. 2017).

The gamma-ray flux from dark matter annihilation or decay depends on the distribution of dark matter within the system (the astrophysical component) and the annihilation cross section or decay rate which determines how the dark matter particles convert into standard model particles (the particle physics component). The astrophysical component that governs the annihilation and decay

fluxes are commonly referred to as the J and D-Factors, which are, respectively, line-of-sight integrals over the dark matter distribution squared and the dark matter distribution within a dSph.

The measured stellar kinematics of dSphs determine the dark matter density distribution, and thereby the J and D-factors. There is a large volume of literature on computing the J and D-factors. The standard methodology for computing these factors for the dSphs involves combining the spherical Jeans equation with a Bayesian likelihood analysis to constrain model parameters (Evans et al. 2004; Strigari et al. 2007, 2008b; Martinez et al. 2009; Charbonnier et al. 2011; Bonnivard et al. 2015a; Geringer-Sameth et al. 2015b; Bonnivard et al. 2015b). The dynamical analyses indicate that the J and D-factors are in particular well-constrained for angular scales subtended by the approximate half-light radius of the stellar system (Walker et al. 2011), which corresponds to an angular scale  $\sim 0.1 - 0.5$  degrees for a typical dSph. The spherical Jeans formalism may be extended to consider an axisymmetric stellar distribution (Hayashi et al. 2016; Klop et al. 2017). The results from the spherical Jeans modeling are consistent with simple analytic relations (Evans et al. 2016) including axisymmetry (Sanders et al. 2016). The astrophysical properties of the global population of dSphs may be used to better constrain the J-factors for individual

\*E-mail: apace@tamu.edu

systems, for example using Bayesian hierarchical modeling (Martinez 2015). The Bayesian techniques used in the aforementioned analyses can be compared to a Frequentist-based method, which is more compatible with the statistical modeling used in the Fermi-LAT gamma-ray analysis (Chiappo et al. 2017).

In recent years, many new dSphs have been discovered in the Sloan Digital Sky Survey (SDSS), PanSTARRS (Laevens et al. 2015a,b), and the Dark Energy Survey (DES) (Bechtol et al. 2015; Koposov et al. 2015a; Drlica-Wagner et al. 2015b). These systems are sufficiently faint that it is difficult to obtain spectroscopy on a large sample of their member stars. Because of these small data samples, and the susceptibility to systematic uncertainties, the velocity dispersion, and therefore the mass and J-factor, may easily be systematically overestimated if the velocity dispersion is based on only a handful of stars (Bonnivard et al. 2016). However, given the importance of the dSphs to dark matter searches, going forward it will be increasingly important to obtain reliable estimates for the J and D-factors, especially for systems without kinematic measurements.

Because many newly-discovered dSphs lack measured stellar kinematics, previous studies have appealed to scaling relations between the J-factor and observable quantities to extract dark matter limits from them. For example Drlica-Wagner et al. (2015a); Albert et al. (2017b) consider a simple model in which the J-factor scales as the inverse of the distance squared to the dSph. This scaling was motivated by the fact that the dSphs have similar integrated dark matter masses, despite having a wide range of luminosities (Strigari et al. 2008a; Walker et al. 2009d; Wolf et al. 2010). As even more dSphs are discovered, it will be increasingly important to identify the most optimal scaling relations between the J and D-factors and the observable properties of the dSphs.

In this paper, we compute the J and D-factors from the dSphs with measured stellar kinematics, and perform new calculations for several systems that do not have published measurements of these quantities. We include not only the Milky Way (MW) satellites, but also dSphs that are satellites of M31, and are in the local field (LF), not bound to either the MW or M31. We perform a statistical analysis to determine the observable quantities, in particular the line-of-sight velocity dispersion ( $\sigma_{\text{los}}$ ), distance ( $d$ ), and stellar scale ( $r_{1/2}$ ), that the J and D-factors scale with. We determine the appropriate scaling relations, and quantify the residuals obtained from these relations. Our statistical analysis builds on the analytic work of Evans et al. (2016), who work out relations for the J-factors in terms of parameters that describe the dark matter halo, such as the scale density and the scale radius.

We structure of this paper as follows. In Section 2, we summarize the dSph properties and data sources. In Section 3, we present our dynamical framework for determining the dark matter distributions and subsequent J and D-Factor calculations. In Section 4, we present results for the galaxy sample, present scaling relations for the J and D-Factors, and discuss some systematics. In Section 5, we conclude.

## 2 DATA

To determine the J and D-factors, we compile a large sample of dSph spectroscopic data from the literature. The sample properties are summarized in Table A1 and includes the distance ( $d$ ), azimuthally averaged half-light radius ( $r_{1/2}$ ), line-of-sight velocity dispersion ( $\sigma_{\text{los}}$ ), absolute magnitude ( $M_V$ ), and number of spectroscopic members ( $N$ ). We have opted not to combine spectroscopic

samples due to potential zero-point offsets in heliocentric velocity between different telescopes/instruments or mis-estimation of velocity errors. We use the Gaussian likelihood given in Walker et al. (2006) to compute the average velocity,  $\bar{V}$ , and  $\sigma_{\text{los}}$ . For  $\sigma_{\text{los}}$  we assume a Jefferys prior with range  $-2 < \log_{10} \sigma_{\text{los}} < 2$ . The resulting values of  $\sigma_{\text{los}}$  are listed in Table A1.

For galaxies not mentioned in the remainder of section the membership is identical to the original study. The data for Carina, Fornax, Sculptor, and Sextans is from in Walker et al. (2009a), the Draco data is from Walker et al. (2015), and the Ursa Minor data from M. Spencer et al. in prep (Matt Walker private communication). For all 6 galaxies, we select member stars by applying a cut at  $p_i > 0.95$ , where  $p_i$  is the membership probability determined from the expectation maximization method (Walker et al. 2009b). For Leo I (Mateo et al. 2008) and Leo II (Spencer et al. 2017b) we use a  $3 - \sigma$  clipping algorithm to select members. This is similar to the selection used in the original analysis.

For Boötes I, we use the 37 member “Best” sample in Koposov et al. (2011). We additionally explored a larger subset of this sample and found consistent results. We have made slight membership changes to the Simon & Geha (2007) data for the following dSphs: Canes Venatici I, Coma Berenices, Leo IV, Ursa Major I, and Ursa Major II. We have removed RR Lyrae from the following (identified after the original spectroscopic analysis): Canes Venatici I (5 RR Lyrae identified in Kuehn et al. 2008), Coma Berenices (1 star; Musella et al. 2009), Leo IV (1 star; Moretti et al. 2009), and Ursa Major I (3 stars; Garofalo et al. 2013). RR Lyrae are pulsating stars with variable velocity; these stars are dSph members, however, we do not know where they are in their phase. In Ursa Major II, a foreground dwarf has been removed that was identified in follow-up high-resolution spectroscopy analysis (Frebel et al. 2010). These removals do not have a large impact as the removed stars tend to have large error bars. For Segue 1, we used the Bayesian membership probability ( $p_i > 0.8$ ) to identify Segue 1 members (Simon et al. 2011).

The Hercules data set has 18 members (Adén et al. 2009) but we have removed one member that was later identified as a spectroscopic binary<sup>1</sup> (Koch et al. 2014). Regarding Hercules it is also worth noting that several studies indicate that this galaxy may be undergoing tidal disruption (e.g. Deason et al. 2012; Küpper et al. 2017; Garling et al. 2018). For Leo V, we use the 8 star data set from Collins et al. (2017). We note that this analysis argued that Leo V contains a large velocity gradient, a potential indication of tidal disruption. For Willman 1, we use the 40 likely members selection but note that the dynamical state of this system is unclear (Willman et al. 2011). Furthermore, Willman 1 member selection is difficult due to the overlap in heliocentric velocity with the MW field stars (Siegel et al. 2008; Willman et al. 2011).

The data for Grus I and Tucana II is from Walker et al. (2016). We find that simply weighting the stars by their reported mean membership values gives a  $\sigma_{\text{los}}$  result that disagrees with the values reported in Walker et al. (2016). We speculate that this disagreement is due to our lack of a Milky Way background model; there are several stars with large errors on the dSph membership probabilities that could be driving the dispersions apart. In order to reproduce the Walker et al. (2016) values, we exclude (include) the two stars in Grus I (Tucana II) with large membership errors but non-zero membership giving a sample of 5 (10) stars.

<sup>1</sup> The binary star’s center of mass velocity was identified but there is a zero point offset between the different studies.

We include a handful of more distant objects in our compilation including five M31 satellites and four local field (LF) objects. We selected the 5 Andromeda satellites with the largest sample size from the SPLASH survey (Tollerud et al. 2012). Following the SPLASH team, dSph stars are selected with a membership probability cut of  $p_i > 0.1$ . The LF objects we include here are: And XVIII (Tollerud et al. 2012,  $d_{\text{M31}} - d_{\text{AndXVIII}} \approx 600\text{kpc}$ ), Cetus (Kirby et al. 2014), Eridanus II (Li et al. 2017), and Leo T (Simon & Geha 2007). We did not consider any other local group dSph/dIrr as our dynamical modeling assumptions are not appropriate; they contain either low mass-to-light ratios (e.g. Aquarius, Leo A, NGC 6822, Kirby et al. 2014), large gas components, disk-like stellar components, peculiar kinematics (e.g. Tucana, Fraternali et al. 2009), and/or stellar rotation (e.g. Pegasus and Phoenix, Kirby et al. 2014; Kacharov et al. 2017).

### 3 METHODS

In this section we briefly outline the method for calculating the J and D-factors. To facilitate comparison with previous results, we follow standard treatments in the literature (e.g. Evans et al. 2004; Strigari et al. 2007, 2008b; Martinez et al. 2009; Charbonnier et al. 2011; Bonnivard et al. 2015a; Geringer-Sameth et al. 2015b; Bonnivard et al. 2015b), and refer to these papers for more details and discussion of systematics.

The J-Factor (annihilation factor) is an integral over the line-of-sight and solid angle of the dark matter density squared:

$$J(\theta_{\max}) = \iint_{\text{los}} \rho_{\text{DM}}^2(r) d\ell d\Omega, \quad (1)$$

where  $\rho_{\text{DM}}$  is the dark matter density profile,  $\ell$  is the line-of-sight direction and  $\Omega$  is the solid angle of radius  $\theta_{\max}$ . The relationship between  $r$  and  $\ell$  is:  $r^2 = \ell^2 + d^2 - 2\ell d \cos \theta$  and  $d\Omega = 2\pi \sin \theta d\theta$ . The limits of the  $\ell$  integration are:  $\ell_{\pm} = d \cos \theta \pm \sqrt{r_t^2 - d^2 \sin^2 \theta}$  and  $r_t$  is the dark matter tidal radius. The D-Factor (decay factor) is:

$$D(\theta_{\max}) = \iint_{\text{los}} \rho_{\text{DM}}(r) d\ell d\Omega. \quad (2)$$

For both the J and D-factor, the key quantity to determine from the stellar photometry and kinematic data is  $\rho_{\text{DM}}$ . The dark matter density is constrained through the spherical jeans equation,

$$\frac{dv\sigma_r^2}{dr} + \frac{2}{r}\beta(r)v\sigma_r^2 + \frac{vGM(r)}{r^2} = 0, \quad (3)$$

where  $v$  is the tracer (stellar) density,  $\sigma_r^2$  is the radial velocity dispersion,  $\beta(r) = 1 - \frac{\sigma_r^2}{2\sigma_t^2}$  is the velocity anisotropy, and  $M(r)$  is the mass profile. Since the dSphs have large mass-to-light ratios (with the only exception being the central region of Fornax), we assume that the mass profile is entirely dominated by the dark matter halo.

To compare  $\sigma_r^2$  to observed line-of-sight velocity data it needs to be projected into the line-of-sight direction. The projection is:

$$\Sigma(R)\sigma_{\text{los}}^2(R) = 2 \int_R^\infty dr \left[ 1 - \beta(r) \frac{R^2}{r^2} \right] \frac{rv\sigma_r^2(r)}{\sqrt{r^2 - R^2}}, \quad (4)$$

where  $\sigma_{\text{los}}$  is the line-of-sight velocity dispersion and  $\Sigma$  the projected tracer density. We model the stellar profile with a Plummer (1911) model. The 3D distribution is:

$$v_{\text{Plummer}}(r) = \frac{3}{4\pi r_p^3} \frac{1}{(1 + (r/r_p)^2)^{5/2}}. \quad (5)$$

and the projected (2D) distribution is:

$$\Sigma_{\text{Plummer}}(r) = \frac{1}{\pi r_p^2} \frac{1}{(1 + (R/r_p)^2)^2}. \quad (6)$$

The Plummer profile has a scale radius,  $r_p$ , which is equivalent to the stellar half-light radius. The dSphs have varying ellipticity ( $\epsilon \approx 0.1 - 0.7$  McConnachie 2012); to approximate spherical symmetry, we use azimuthally averaged half-light radii:  $r_{1/2} = r_{\text{half, azimuthal}} = r_{\text{half, major}} \sqrt{1 - \epsilon}$ . When referring to the half-light radius ( $r_{1/2}$ ), we are referring to the azimuthally averaged value. Note that it is possible to consider more generalized models than the Plummer profile (Strigari et al. 2010), however this is an unnecessary complication for our analysis. We parameterize the dark matter distribution as a NFW profile (Navarro et al. 1996):

$$\rho_{\text{DM}} = \frac{\rho_s}{x(1+x)^2}, \quad (7)$$

where  $x = r/r_s$ , and the scale radii and density are  $r_s$  and  $\rho_s$  respectively.

To extract the model parameters from the data, we use an unbinned likelihood function (Strigari et al. 2008b; Martinez et al. 2009; Geringer-Sameth et al. 2015b):

$$\mathcal{L}_v(\mathcal{D}) = \prod_{i=1}^N \frac{p_i}{\sqrt{2\pi(\sigma_{\text{los}}^2(R_i) + \sigma_{\epsilon,i}^2)}} \exp \left[ -\frac{1}{2} \frac{(V_i - \bar{V})^2}{\sigma_{\text{los}}^2(R_i) + \sigma_{\epsilon,i}^2} \right], \quad (8)$$

Here each data point is the radial position, line-of-sight velocity, velocity error, and membership probability;  $\mathcal{D}_i = (R_i, V_i, \sigma_{\epsilon,i}, p_i)$ . For many sets  $p_i = 1$  and the original analysis will need to be consulted for additional information.

For the classical MW satellites with measured proper motions, we also account for the perspective motion effect outlined in Kaplinghat & Strigari (2008); Walker et al. (2008). Briefly, for a large extended object (i.e. a “classical” dSph), only at the center of the object do the line-of-sight and z-directions exactly align. A small component of the line-of-sight velocity comes from the net proper motion of the galaxy; this effect increases the further from the center. Note this is generally a small effect, corresponding to  $1 - 2 \text{ km s}^{-1}$ . The proper motions (in mas century $^{-1}$ ) of the classical satellites are as follows ( $\mu_\alpha \cos \delta, \mu_\delta$ ):  $(22 \pm 9, 15 \pm 9)$  (Carina; Piatek et al. 2003),  $(5.62 \pm 0.99, -16.75 \pm 1.0)$  and  $(2.96 \pm 2.09, -13.58 \pm 2.14)$  (Draco and Sculptor; Sohn et al. 2017),  $(47.6 \pm 4.5, -36.0 \pm 4.1)$  (Fornax; Piatek et al. 2007),  $(-11.4 \pm 2.95, -12.56 \pm 2.93)$  (Leo I; Sohn et al. 2013),  $(-6.9 \pm 3.7, -8.7 \pm 3.9)$  (Leo II; Piatek et al. 2016),  $(-40.9 \pm 5.0, -4.7 \pm 5.8)$  (Sextans; Casetti-Dinescu et al. 2017), and  $(-50 \pm 17, 22 \pm 16)$  (Ursa Minor; Piatek et al. 2005). When available, we choose proper motion results based on data from the *Hubble Space Telescope* over ground based studies.

We determine the posterior distributions with the MultiNest sampling routine (Feroz & Hobson 2008; Feroz et al. 2009). We assume Gaussian priors on distance, half-light radius, ellipticity, and the proper motions (for classical satellites). Whenever possible we use the half-light radius derived from Plummer fits or exponential fits. For several brighter satellites, we have determined the half-light radius from King fits using the formula in the Appendix of Wolf et al. (2010). To approximate Gaussianity, some parameter

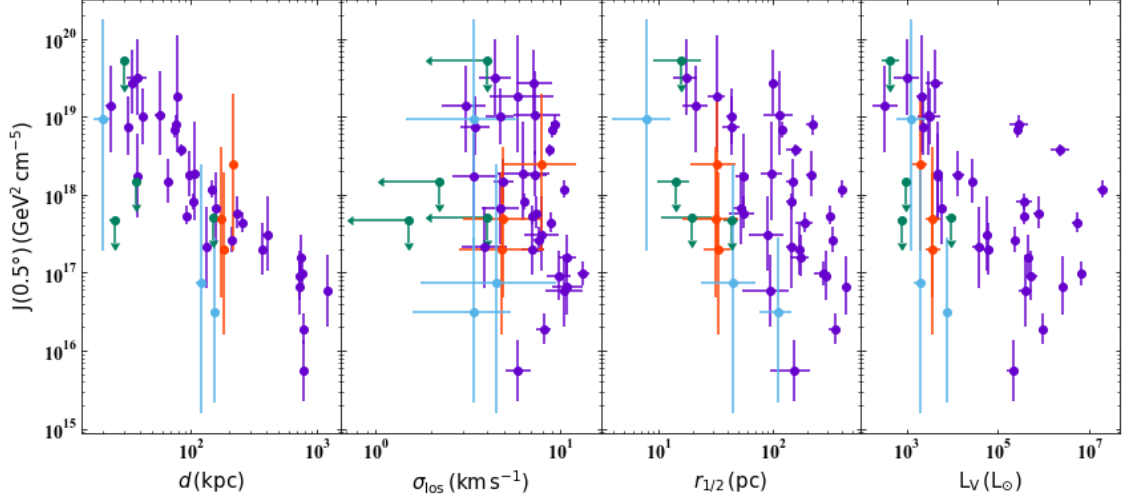


**Figure 1.** J-Factor within a solid angle of  $0.5^\circ$  versus (from left to right): distance ( $d$ ; kpc), velocity dispersion ( $\sigma_{\text{los}}$ ; km/s), azimuthally averaged half-light radius ( $r_{1/2}$ ; pc), and luminosity ( $L_V$  ( $L_\odot$ )). The dSphs are separated based on whether the velocity dispersion is resolved. Purple points are resolved while green upper limits are unresolved. The orange and light blue points have small and large tails to zero velocity dispersion but contain a clear peak in their posterior (see text for additional details). Only the peak is displayed.

errors represent the average of the upper and lower error bars<sup>2</sup>. We assume a uniform prior range for  $\bar{V}$ :  $-10 \leq \bar{V} - V_{\text{literature}} \leq +10$ <sup>3</sup>. Jeffreys' priors are assumed for the dark matter halo parameters:  $-2 \leq \log_{10} r_s \leq 1$ , and  $4 \leq \log_{10} \rho_s \leq 14$ . We additionally assume that  $r_s > r_{1/2}$  (see Section 4.1 of [Bonnivard et al. 2015a](#), and discussion in Section 4.2).

We take the velocity anisotropy to be constant with radius,  $\beta(r) = \beta_0$ . Instead of a prior in linear  $\beta$  space, we parameterize the anisotropy in a symmetrized space;  $\tilde{\beta} = \beta / (2 - \beta)$  (see Eq. 8 in [Read et al. 2006](#); [Read & Steger 2017](#)). The symmetrized parameterization uniformly favors radial and tangential orbits whereas the linear parameterization preferentially samples tangential orbits<sup>4</sup>. The prior range is  $-0.95 \leq \tilde{\beta} \leq 1$ .

The dark matter tidal radius,  $r_t$ , is required for the J and D-Factor calculation. We compute  $r_t$  via:  $r_t = [M_{\text{sub}}(r_t) / (2 - d \ln(M_{\text{host}}) / d \ln r) M_{\text{host}}(d)]^{1/3} d$  (Eq. 12 of [Springel et al. 2008](#)). The MW and M31 host mass profiles are from [Eadie & Harris \(2016\)](#) and [Sofue \(2015\)](#) respectively. The LF objects and unresolved  $\sigma_{\text{los}}$  systems have  $r_t$  fixed to  $r_t = 25$  kpc and  $r_t = 1$  kpc respectively.

## 4 RESULTS AND DISCUSSION

We compute the J and D-Factors within solid angles of  $\theta_{\text{max}} = 0.1^\circ, 0.5^\circ, \alpha_c$ , where  $\alpha_c$  is the angle within which the uncertainties

<sup>2</sup> We note that it is better to redraw the measured parameter distributions directly from the posterior distributions. In most cases these are not available but they are from M31 distances ([Conn et al. 2012](#)) and M31 structural parameters ([Martin et al. 2016b](#)). For additional discussion on this topic see [Martin et al. \(2016b\)](#).

<sup>3</sup> This prior range is expanded for several satellites with small sample sizes.

<sup>4</sup> Another alternative anisotropy parameterization for equally favoring radial and tangential orbits is:  $\beta' = \log_{10}(1 - \beta)$  ([Charbonnier et al. 2011](#)).

are minimized for J and D-Factor analyses ([Walker et al. 2011](#)). The J-Factor angle is  $\alpha_c = 2r_{1/2}/d$ , while for the D-Factor value is half the J-Factor  $\alpha_c^D = \alpha_c/2$ . We provide the first J and D-Factor analysis for the recently discovered MW dSphs Aquarius II and Pegasus III. We also provide the first J and D-factor analyses for the M31 satellites and a couple of the dispersion supported local group objects (And XVIII and Cetus). Surprisingly, even though it is at a relatively large distance, And VII has a J-Factor comparable to some “faint” MW satellites and therefore will be useful in future combined gamma-ray likelihood analyses<sup>5</sup>.

In Figure 1, we show a summary of the integrated J-Factors within  $0.5^\circ$  for our sample. From these results we can test how the J-Factor scales with the following observed dSph properties:  $d$ ,  $\sigma_{\text{los}}$ ,  $r_{1/2}$ , and V-band luminosity,  $L_V$ . We separate the dSphs into four categories based the resolution of  $\sigma_{\text{los}}$ : resolved systems (purple), systems with small  $\sigma_{\text{los}}$  tails (orange), marginally resolved systems (light blue), and unresolved systems (green upper limits). The intermediate sub-sets have tails in the  $\sigma_{\text{los}}$  and J-Factor posterior to small values (equivalent to zero) and we have removed this part of the posterior to compare the “resolved” portion to other dSphs. We discuss these systems in more detail in Section 4.1. Since the J-Factor is essentially a “flux,” it therefore scales as the inverse of distance squared, as observed in the  $d$  subplot. The  $d$  sub-plot shows the expected inverse-squared scaling, justifying the previously-used simple scaling models ([Drlica-Wagner et al. 2015a](#); [Albert et al. 2017b](#)). In Figure 2 we compare the J-Factors at the four different integration angles ( $0.1^\circ, 0.2^\circ, 0.5^\circ$  and  $\alpha_c$ ) versus  $d$ .

For several of the recently-discovered dSphs in DES

<sup>5</sup> In principle most M31 satellites and local group dwarf irregular galaxies could be added to stacked analysis. This has been discussed within the dynamical framework of rotation curve modeling for local field dwarf irregular galaxies ([Gammaldi et al. 2017](#)).

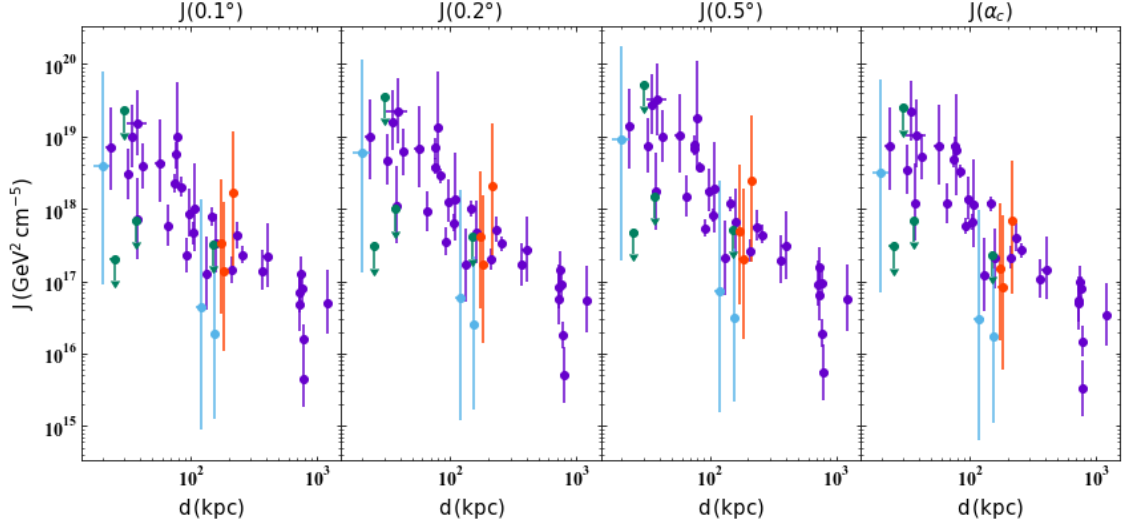


**Figure 2.** J-Factor versus distance for integration angles of  $0.1^\circ$ ,  $0.2^\circ$ ,  $0.5^\circ$ , and  $\alpha_c$ .  $\alpha_c$  is the angle where the J-Factor uncertainties are minimized (Walker et al. 2011).

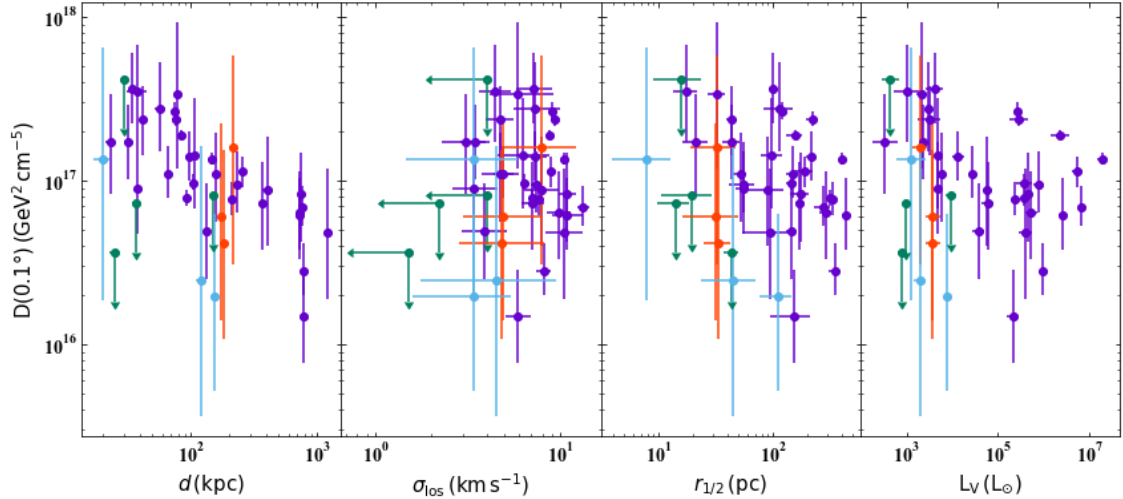


**Figure 3.** Same as Figure 1 except with the J-Factor replaced with the D-Factor within  $0.1^\circ$ .

(Horologium I, Reticulum II, and Tucana II) the stellar parameters differ between the two independent discovery analyses (Bechtol et al. 2015; Koposov et al. 2015a). We compute the J-Factors for these objects with both sets of stellar parameters (results for both are listed in Table A1). The differences in J-Factor are  $\Delta \log_{10}(J(0.5^\circ)) \sim 0.4, 0.1, 0.2$  for the three galaxies respectively. The largest difference is found in Horologium I where there is a factor of two difference in  $r_{1/2}$  between the photometric studies. This suggests that there is some J-Factor scaling with  $r_{1/2}$  despite the lack of an apparently obvious trend in Figure 1. Throughout the remainder of this analysis we will use J and D-Factor values derived with photometric properties from Bechtol et al. (2015).

Deeper photometric data will be particularly important to precisely measure the structural parameters for these galaxies.

In Figure 3 we show the D-Factor within  $0.1^\circ$  versus  $d$ ,  $\sigma_{\text{los}}$ ,  $r_{1/2}$ , and  $L_V$ . There is an inverse squared scaling with  $d$  but it is less pronounced than the trend with J-Factor. The more distant systems contain a larger fraction of the dark matter halo within the fixed integration angles and the D-Factor falls off less rapidly than the J-Factor with  $\theta_{\text{max}}$ .

#### 4.1 Unresolved Velocity Dispersions

As previously mentioned, there are several objects for which a non-negligible portion of the  $\sigma_{\text{los}}$  posterior tends to zero. For

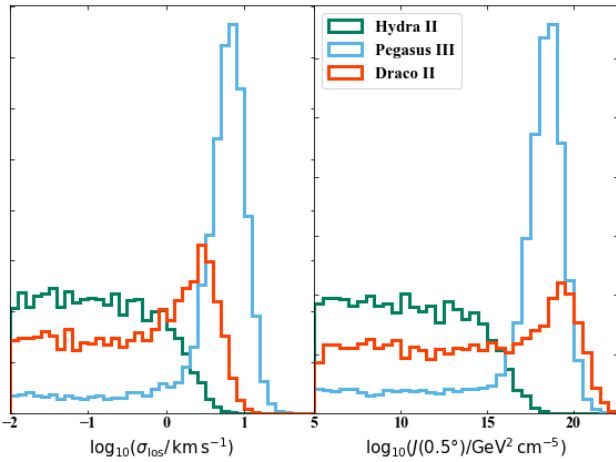


**Figure 4.** Left: Example of three galaxies with (partially) unresolved velocity dispersions. Hydra II (green) contains an upper limit, while Draco II (orange) contains a large zero-dispersion tail and Pegasus III (light blue) has a small tail. Right: The corresponding J-Factors. All histograms are normalized such that the area is unity. In the text we discuss several other dSphs with similar unresolved or partially resolved velocity dispersions.

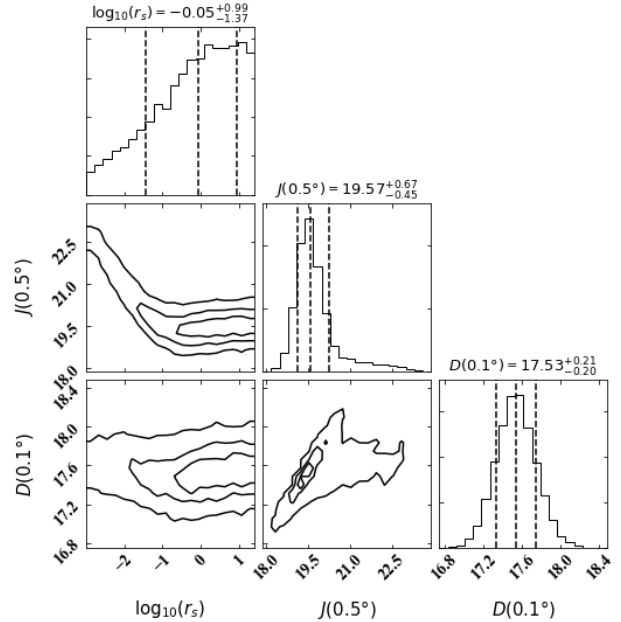


**Figure 5.** Example of posterior without  $r_s > r_{1/2}$  prior. The corner plot compares  $\log_{10} r_s$ ,  $\log_{10} J(0.5^\circ)$  and  $\log_{10} D(0.1^\circ)$  of Ursula Major II. At small  $r_s$ , the J-Factor is systematically larger which is removed with our  $r_s > r_{1/2}$  prior.

several systems the  $\sigma_{\text{los}}$  posteriors are entirely upper limits (Hydra II, Segue 2, Triangulum II, Tucana III; Kirby et al. 2015, 2013, 2017; Simon et al. 2017), while others have large tails to zero- $\sigma_{\text{los}}$  (Draco II, Leo IV, Grus I; Martin et al. 2016a; Simon & Geha 2007; Walker et al. 2016), or small tails (Leo V<sup>6</sup>, Pegasus III, Pisces II; Walker et al. 2009c; Collins et al. 2017; Kim et al. 2016; Kirby et al. 2015). The tails are easily observed in  $\log_{10} \sigma_{\text{los}}$  space and may have been previously overlooked if only examined in linear space.

For these systems, we have expanded the prior range of the dark matter scale density ( $0 < \log_{10} \rho_s < 13$ ) to better illuminate the zero J-factor tail in the posterior (with the original prior only a small portion of the posterior corresponds to zero- $\sigma_{\text{los}}$ ). Note that  $\rho_s$  values in the expanded prior range are highly disfavored from cosmological N-Body simulations (Springel et al. 2008).

In Figure 4, we show  $\sigma_{\text{los}}$  and J-Factor posteriors for representative galaxies from the three cases. A non-resolution of all or part of  $\sigma_{\text{los}}$  implies a similar non-resolution in the J-factor posterior. Note that both posterior distributions will extend to even smaller values if the prior range is expanded. The lower limit of  $\rho_s$  will set the inferred confidence intervals of the J and D-Factors and confidence intervals for these galaxies should be treated with caution. For the subset of galaxies with zero- $\sigma_{\text{los}}$  tails we quote maximum posterior values and error bars encompass the non-tail portion of the posterior in Table A1. For unresolved systems we quote an upper limit at the 99.5% percentile confidence interval after applying a cut at  $\log_{10} \rho_s > 4$ . This allows for better comparison to the remainder of our sample and to previous studies. We exclude the systems with non-resolved  $\sigma_{\text{los}}$  from the global analysis in the remainder of this work.

## 4.2 Halo Priors

In our analysis we have imposed a prior  $r_s > r_{1/2}$  (as suggested by Bonnivard et al. 2015a). To quantify the effect of this prior, we re-analyze several galaxies (Boötes I, Carina II, Reticulum II, Ursula Major II, Draco, and Leo II) without this prior and expand the  $r_s$  prior range ( $-3 < \log_{10} r_s < 1.4$ ). While there is no change for the Draco values (the posterior favors larger  $r_s$  values) all other galaxies show an increase in the J-Factor and most show a decrease in the D-Factor. This effect is generally larger in the ultra-faint galaxies as the halo properties are more likely to be prior dominated. As an example, Figure 5 shows a corner plot comparing the posteriors of  $r_s$ ,  $J(0.5^\circ)$ , and  $D(0.1^\circ)$  for Ursula Major II. For  $r_s > r_{1/2}$ , there is little to no  $r_s$  trend with the J-Factor in contrast to the  $r_s < r_{1/2}$  region.

With mock data sets, Bonnivard et al. (2015a) found that the J-Factor was systematically over-estimated without the  $r_s > r_{1/2}$  prior (see their Section 4.1). Our results for prior dominated systems agree with this result. This is consistent with galaxy formation simulations, in which galaxies form with  $r_s > r_{1/2}$ . In particular for ultra-faint galaxies, the small  $r_s$  values are significantly disfavored by  $\Lambda$ CDM N-Body simulations. For example, the median  $r_s$  values for a halos with  $V_{\text{max}} = 5 - 15 \text{ km s}^{-1}$  are  $r_s = 120 - 600 \text{ pc}$  (Garrison-Kimmel et al. 2014). The systematic over-estimation in the J-Factor, and disagreement with N-body simulations, justifies the  $r_s > r_{1/2}$  prior.

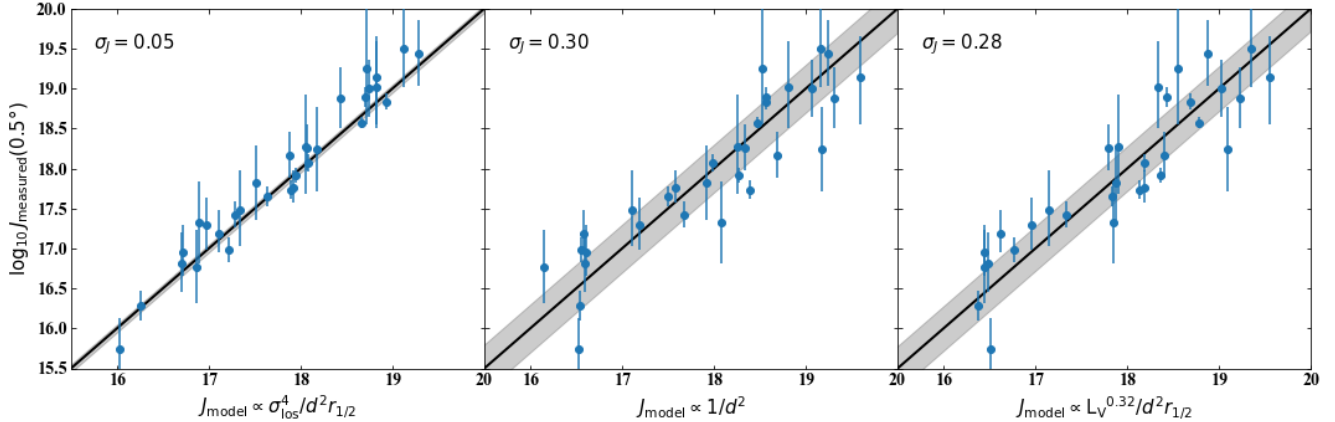


**Figure 6.** J-Factor models versus measured J-Factors at  $\theta_{\max} = 0.5^\circ$ . The models from left to right are:  $\sigma_{\text{los}}^4/d^2r_{1/2}$ ,  $1/d^2$ ,  $L_V^{0.32}/d^2r_{1/2}$ . Each model has been scaled to match the one-to-one line. The shaded bands show the intrinsic spread of the models ( $\sigma_J$ ) which is labeled in the upper-left hand corners. The last model is explored in Section 4.7. The  $\sigma_{\text{los}}$  based model presents a significant improvement over  $1/d^2$  models.

**Table 1.** Normalization ( $J_0/D_0$ ) and intrinsic spread ( $\sigma_J/\sigma_D$ ) (in logarithmic units) of the scaling relations for different integration angles of the J and D-Factors. The units of J(D)-Factor are  $\text{GeV}^2 \text{cm}^{-5}$  ( $\text{GeV} \text{cm}^{-2}$ ).

	$\log_{10} J_0 / \log_{10} D_0$	$\sigma_J/\sigma_D$
$J(0.1^\circ)$	17.51	0.10
$J(0.2^\circ)$	17.63	0.07
$J(0.5^\circ)$	17.72	0.05
$J(\alpha_c)$	17.62	0.05
$D(0.1^\circ)$	9.55	0.53
$D(0.2^\circ)$	9.90	0.47
$D(0.5^\circ)$	10.27	0.37
$D(\alpha_c/2)$	9.32	0.11

### 4.3 J-Factor Scaling

The first searches for dark matter annihilation into gamma-rays from new dwarf galaxy candidates discovered in DES (Bechtol et al. 2015; Koposov et al. 2015a; Drlica-Wagner et al. 2015b) used an empirical scaling relationship between the J-Factor and distance to estimate the J-Factor for the new discoveries (Drlica-Wagner et al. 2015a; Albert et al. 2017b). Their relation is written as  $\log_{10}(J_{\text{pred}}(0.5^\circ)/J_0) = -2\log_{10}(d/100\text{kpc})$ . The normalization,  $J_0$ , varies based on the J-Factor compilation and it ranges between  $\log_{10}J_0 = 18.1 - 18.4 \text{ GeV}^2 \text{cm}^{-5}$  (Geringer-Sameth et al. 2015b; Bonnivard et al. 2015b; Martinez 2015). One of the recently discovered dSphs, Carina II, contained a significantly lower J-Factor than the distance scaling prediction (T. S. Li et al., in prep) and led us to explore more general scaling relations.

Guided by the analytic work of Evans et al. (2016), we examined scaling relations of the form:  $\log(J(\theta_{\max})/J_0) = \alpha \log \sigma_{\text{los}} + \beta \log d + \gamma \log r_{1/2}$ . The best fit scaling parameters ( $\alpha, \beta, \gamma$ ) were determined by examining model residuals and looking for parameterizations without trends with respect to  $d$ ,  $\sigma_{\text{los}}$ , or  $r_{1/2}$ . We quantified the size of the residuals (which we refer to as the intrinsic

spread or scatter with logarithmic units),  $\sigma_J$ , by applying the candidate relation and fitting the residuals with a Gaussian.

We find a minimum in  $\sigma_J$  for model parameters:  $(\alpha, \beta, \gamma) = (4, -2, -1)$  (with  $\theta_{\max} = 0.5^\circ$ ). With typical dSph properties, our J-Factor scaling relation can be expressed as:

$$\frac{J(0.5^\circ)}{\text{GeV}^2 \text{cm}^{-5}} \approx 10^{17.72} \left( \frac{\sigma_{\text{los}}}{5 \text{km s}^{-1}} \right)^4 \left( \frac{d}{100 \text{kpc}} \right)^{-2} \left( \frac{r_{1/2}}{100 \text{pc}} \right)^{-1}. \quad (9)$$

This relation has  $\sigma_J = 0.05$ . We note that  $\sigma_{\text{los}}^4/d^2r_{1/2}$  combined with  $1/G^2$  (Newton's constant) has the units of the J-Factor, as the units of  $[J/G^2]$  are  $[\text{velocity}]^4/[\text{length}]^3$ . In Table 1, we list normalization ( $J_0$ ) and  $\sigma_J$  for other integration angles. The minimum  $\sigma_J$  occurs at  $0.5^\circ$  and  $\alpha_c$ . We expect the minimum to occur at  $\alpha_c$  as it is dependent on the  $r_{1/2}$ , the radius where the mass is best estimated for dispersion supported systems (Walker et al. 2009d; Wolf et al. 2010). The errors in the J-Factors are minimized at this angle (Walker et al. 2011). Due to the rapid fall-off of the J-Factor with  $\theta_{\max}$ , it is not surprising to see small scatter at the larger angle also.

In Figure 6, we compare J-Factor models and measurements (at  $\theta_{\max} = 0.5^\circ$ ). The models from left to right are:  $\sigma_{\text{los}}^4/d^2r_{1/2}$ ,  $1/d^2$ ,  $L_V^{0.32}/d^2r_{1/2}$ . Each model is scaled to match the one-to-one line. The first is our best-fit model and has the smallest  $\sigma_J$ . The second is the previously utilized distance based model (Drlica-Wagner et al. 2015a; Albert et al. 2017b). The last is a luminosity based model and is discussed in detail in Section 4.7. As shown in Figure 6, the  $\sigma_{\text{los}}$  based scaling relation provides an excellent fit to the data.

In Figure 7, we show the residuals ( $J_{\text{measured}} - J_{\text{model}}$ ) of this relationship along with subsets of the parameters. We compare the residuals versus  $d$ ,  $\sigma_{\text{los}}$ ,  $r_{1/2}$ , and  $L_V$ , where  $L_V$  acts as a cross-check and is not a direct input. For ease of comparison, each row has the same residual range (y-axis) and shaded bands display  $\sigma_J$  for each model. In all subset panels, there are trends with respect to the “missing” dSph parameters. The rough form of our relation can be derived by examining several rows in Figure 7. The first step is to examine the  $d$  only relation (second row of Figure 7) and observe that the residuals have a positive trend with  $\sigma_{\text{los}}$ . The  $\sigma_{\text{los}}^4/d^2$  relation (fifth row in Figure 7), has a negative trend with

<sup>6</sup> In Leo V we find a similar small zero- $\sigma_{\text{los}}$  tail in the 5 star data set from Walker et al. (2009c).

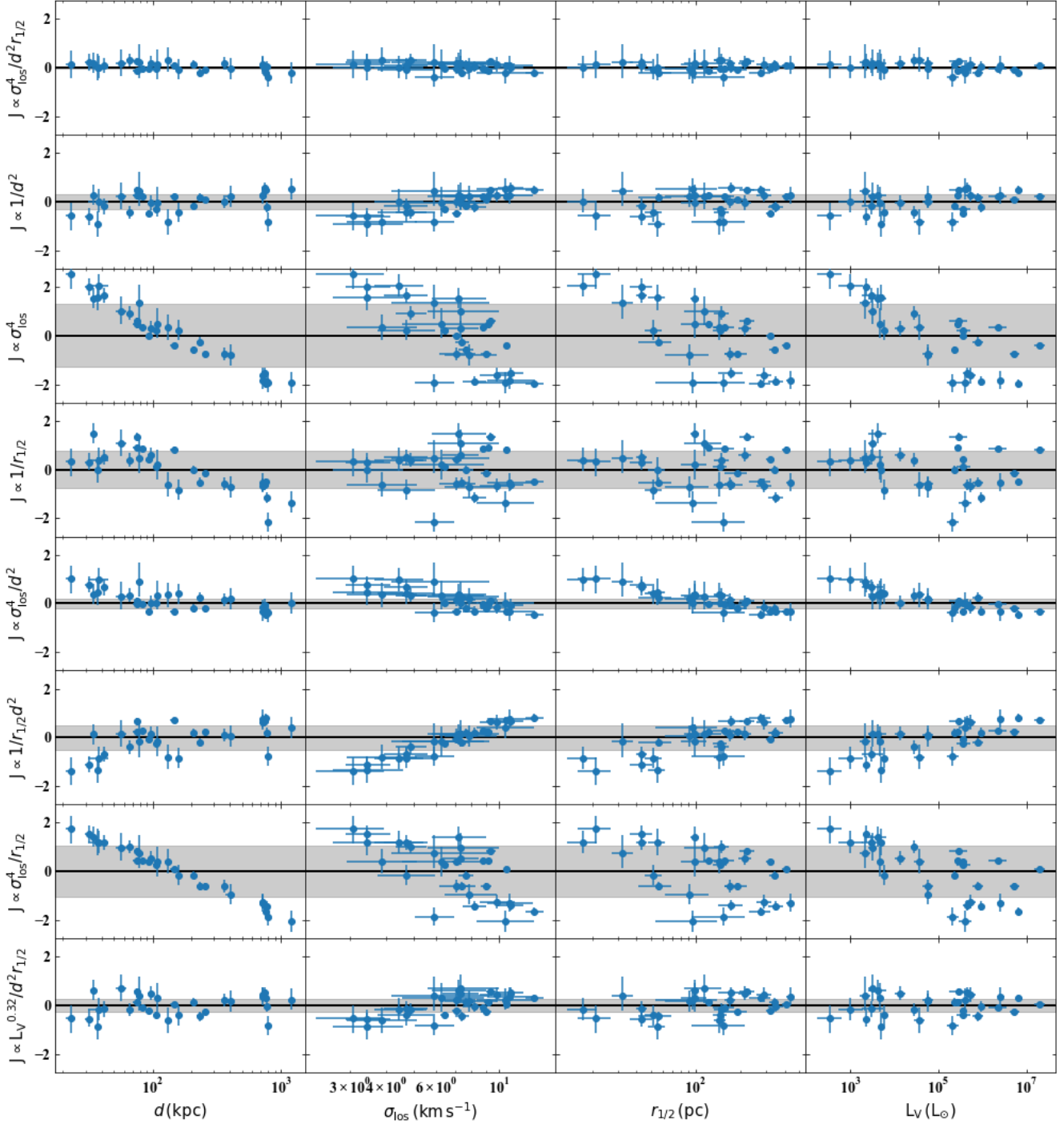


**Figure 7.** The residuals ( $J_{\text{measured}} - J_{\text{model}}$ ; y-axis) with several different J-Factor (with  $\theta = \alpha_c$ ) models versus distance ( $d$ ), azimuthally average half-light radius ( $r_{1/2}$ ), velocity dispersion ( $\sigma_{\text{los}}$ ), and luminosity ( $L_V$ ). The models are listed on the y-axis and from top to bottom they are:  $J \propto \sigma_{\text{los}}^4/d^2 r_{1/2}$ ,  $1/d^2$ ,  $\sigma_{\text{los}}^4$ ,  $1/r_{1/2}$ ,  $\sigma_{\text{los}}^4/d^2$ ,  $1/d^2 r_{1/2}$ ,  $\sigma_{\text{los}}^4/r_{1/2}$ , and  $L_V^{0.32}/d^2 r_{1/2}$ . The bands shows intrinsic scatter ( $\sigma_J$ ) of each model assuming there is no dependence on any parameter. The y-axis displays the same total range for each relationship. Non-constant residuals indicate the candidate model is incorrect.

$r_{1/2}$ . When examining the full relation (top row), there are no trends in the residuals.

The best fit power of  $\sigma_{\text{los}}$  is large compared to the other parameters and there is no apparent trend with respect to  $\sigma_{\text{los}}$  in Figure 1. This is due to the small dynamic range of  $\sigma_{\text{los}}$  in the dSphs.

In particular,  $\sigma_{\text{los}}$  only varies by an order of magnitude ( $3 \lesssim \sigma_{\text{los}} \lesssim 11 \text{ km s}^{-1}$ ), whereas the other parameters vary by several orders of magnitude ( $20 \lesssim d \lesssim 1200 \text{ kpc}$  and  $20 \lesssim r_{1/2} \lesssim 600 \text{ pc}$ ). As  $r_{1/2}$  has the weakest scaling in the  $J$ -factor relation, the trend is only marginally observable in Figure 1 whereas the  $d$  scaling is appar-

ent. Since the range in  $\sigma_{\text{los}}$  between the dSphs is relatively small, the large  $\sigma_{\text{los}}$  power is not seen until the other trends are removed (sixth row in Figure 7). We note that the exponent in the  $\sigma_{\text{los}}$  scaling has larger uncertainty than the other parameters; the parameter range  $\alpha = 3.5 - 4.5$  has little variation with respect to the median value. The large uncertainty is due to the small dynamic range of  $\sigma_{\text{los}}$  values.

As a cross-check we explored computing the scaling relation parameters ( $J_0$ ,  $\sigma_J$ ) with various sub-sets of our sample. In particular, we separated the sample based on luminosity ( $L_V \leq 10^{4.5} L_\odot$ ), host (MW or M31 + LF), or a pre-DES sample (specifically galaxies used in [Geringer-Sameth et al. 2015b](#)). In general, we find the similar values for most sub-sets ( $\Delta J_0 \approx 0.02$  and  $\Delta \sigma_J \approx +0.02$ ) however, the faint subset and the distant sample (M31 + LF) have slightly larger  $\sigma_J$  values and larger/smaller  $J_0$  values respectively. The different in  $J_0$  is likely driven by the distance clustering in these subsets.

#### 4.4 D-Factor Scaling

We turn now to deriving a D-Factor scaling relation. The best fit scaling relation with typical dSph parameters is:

$$D(\alpha_c/2) \approx 10^{16.75} \left( \frac{\sigma_{\text{los}}}{5 \text{ km s}^{-1}} \right)^2 \left( \frac{100 \text{ kpc}}{d} \right)^2 \left( \frac{r_{1/2}}{100 \text{ pc}} \right), \quad (10)$$

and has  $\sigma_D = 0.11$ . The coefficients for the other D-Factor angles are listed in Table 1. For the D-Factor, the only scaling relation model angle with small scatter is  $\alpha_c/2$ . The relationship for the D-Factor has considerably larger scatter than the J-Factor scaling. This is due to the shape of the D-Factor integrand with respect to  $\theta$  (only line-of-sight integration) compared to the analogous J-Factor integrand. For the J-Factor integrand the majority of “signal” comes within  $r_s$  and always decreases with respect to  $\theta$ . For the D-Factor however, the integrand initially increases with respect to  $\theta$  and then turns over  $\theta \approx 0.4r_s/d$ . There is significantly slower falloff with  $\theta$  for the D-Factor than for the J-Factor. At a fixed integration angle, the shape of the D-Factor integrand will vary between objects, whereas it takes a similar shape in the J-Factor for all objects. The D-Factor profile dependence increases the scatter in all scaling relations at fixed integration angle with respect to the J-Factor. In Figure 8, we present the D-Factor residual plot. Similar to the J-Factor scaling relation, when a sub-set of the parameters is examined the residuals are correlated.

#### 4.5 Analytic Relation

We can derive the form of our scaling relation by appealing to the analytic work of [Evans et al. \(2016\)](#). They derive analytic J and D-Factors for several simple halo profiles including the NFW profile. Their analytic J and D-Factors contain two, generally valid, simplifying assumptions: first, the dwarf is distant enough to simplify the angular part of the integration (projection from infinite distance versus finite distance) and second, the dark matter halo has no truncation radius (infinite  $r_t$ ). We find that their formula works remarkably well for the NFW J-Factor; generally, the percent error between the numerical integration and approximate analytic calculation in our posterior distribution is  $\leq 0.1\%$ . The D-Factor formula however, performs quite poorly due to the infinite tidal radius assumption (percent errors range from 1 – 50%). As the D-Factor has a larger dependence on the total size of the dark matter

halo than the J-Factor, the approximation tends to over estimate the D-Factor. We therefore only focus on the analytic J-Factor work.

The bulk of our derivation is in Appendix A. Briefly, we start with the analytic J-Factor formula for the NFW profile in [Evans et al. \(2016, Equation 16\)](#) and replace the halo scale density with observed quantities ( $\sigma_{\text{los}}$ ,  $r_{1/2}$ ) using the half-mass estimators ([Walker et al. 2009d; Wolf et al. 2010](#)). At  $\alpha_c$ , the J-Factor can then be written as:

$$J(\alpha_c) = \frac{\sigma_{\text{los}}^4}{G^2 d^2 r_{1/2}} F(r_{1/2}/r_s), \quad (11)$$

where the  $F$  is an analytic function derived in the appendix. The  $\sigma_{\text{los}}^4$  dependence comes from the half-mass estimators ( $J \propto \rho_s^2 \propto M^2 \propto \sigma_{\text{los}}^4$ ) and  $d^{-2}$  dependence from the “flux” nature of the J-Factor. The remaining unit is  $1/[\text{length}]$  and implies that  $J \propto 1/r_{1/2}$ . The first part of Equation 11 is the scaling relation we find while the remainder is dependent on the ratio  $r_{1/2}/r_s$ . With  $\langle r_{1/2}/r_s \rangle \approx 0.25$ , Equation 11 has the same normalization as our scaling relations for  $\alpha_c$  (see Table 1).

#### 4.6 Comparison with other J-Factor Compilations

As a cross check we examine whether the compilation of [Geringer-Sameth et al. \(2015b\)](#) obeys the same scaling relation<sup>7</sup> (Equation 9). They provide tabulated values for the  $d$  and  $r_{1/2}$  used in their analysis, which allows for a straightforward comparison with our results. The primary difference between their J-Factor analysis and ours is that their analysis assumes a generalized dark matter halo, but has the same stellar anisotropy and stellar density profile assumptions.

We find that the same scaling relation describes their compilation of J-Factors, however, we find that the normalization is slightly larger ( $\log(J_0) = 17.89$  versus our  $\log(J_0) = 17.72$ ) and the spread is slightly increased ( $\sigma_J = 0.08$  versus our  $\sigma_J = 0.05$ ). If we limit our compilation to only the galaxies in the [Geringer-Sameth et al.](#) analysis we find the same normalization and scatter as in our original sample. The difference in normalization between the compilations is likely due by the different dark matter profiles used. This implies that our scaling relation results are robust to changing the dark matter profile

#### 4.7 Scaling with Luminosity

In the era of deep and wide surveys, it will become increasingly more difficult for the rate at which stellar kinematics are measured within individual systems to keep up with the rate at which new systems are discovered. So it is important to determine how the J and D-factors scale with parameters other than  $\sigma_{\text{los}}$ . For satellites without stellar kinematics, the stellar luminosity,  $L_V$ , may be a potential replacement for  $\sigma_{\text{los}}$ . In our dSph sample, there is a correlation between  $\sigma_{\text{los}}$  and  $L_V$ . Replacing  $\sigma_{\text{los}}$  with  $L_V$ , the best fit scaling relation we find is (we fixed the power of  $d$  and  $r_{1/2}$ ):

$$\frac{J(0.5^\circ)}{\text{GeV}^2 \text{cm}^{-5}} \approx 10^{17.93} \left( \frac{L_V}{10^4 L_\odot} \right)^{0.32} \left( \frac{d}{100 \text{ kpc}} \right)^{-2} \left( \frac{r_{1/2}}{100 \text{ pc}} \right)^{-1}. \quad (12)$$

<sup>7</sup> We exclude the galaxies Leo IV, Leo V, and Segue 2 in their sample from this cross-check.

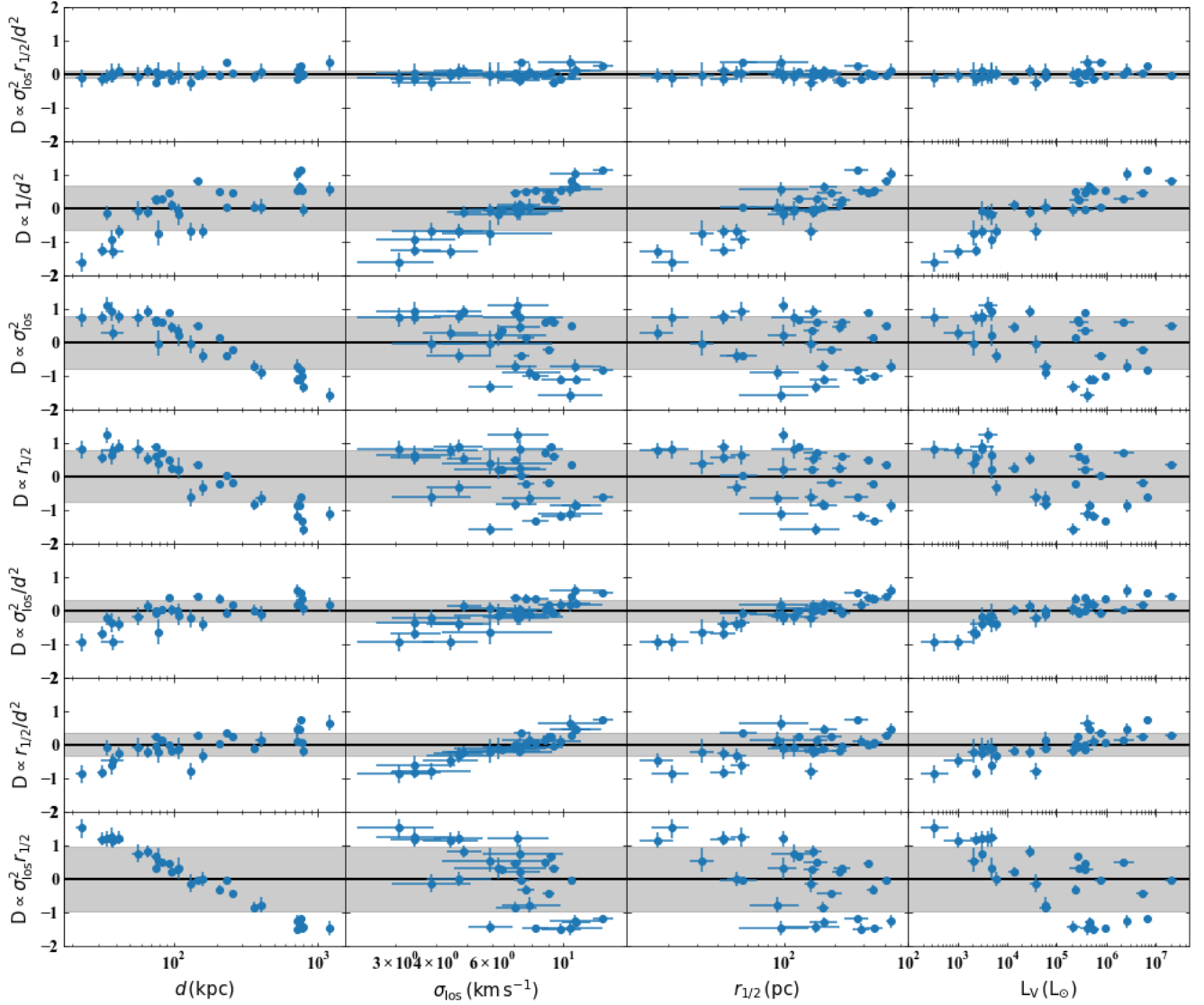


**Figure 8.** Same as Figure 7, except with D-Factor models at  $\theta = \alpha_c/2$  instead of J-Factor models.

This scaling relation has an intrinsic scatter of  $\sigma_J = 0.28$ , which is larger than the scaling with  $\sigma_{\text{los}}$  ( $\sigma_J = 0.05$ ), but it is equivalent in scatter to a simple  $d^{-2}$  scaling ( $\sigma_J = 0.29$ ). The residuals additionally correlate with  $\sigma_{\text{los}}$  and we were not able to remove this correlation (see last row of Figure 7). We additionally test different subsets of our sample to check if this result is driven by any particular range in luminosities. In sub-sets with low luminosity galaxies removed (specifically the sub-sets are at  $\log_{10} L_V < 3.5, 4.0, 4.5$ ) there is essentially no change in the intrinsic scatter. Similarly, there is minimal change in the intrinsic scatter when examining only the ultra low-luminosity galaxies ( $\log_{10} L_V < 4.5$ ) or only MW galaxies.

There are a couple caveats to note with the above results. Many of the M31 dSphs with smaller kinematic samples do not follow the same  $L_V - \sigma_{\text{los}}$  trend as the dSphs in our sample (Tollerud et al. 2012; Collins et al. 2013). The recently discovered diffuse galaxy, Crater II, also falls below this relationship (Torrealba et al. 2016a; Caldwell et al. 2017). However, note that our  $\sigma_{\text{los}}$  relation-

ship predicts  $\log_{10} J(0.5^\circ) = 15.5$ , while the only published measurement is at a larger angle and is  $\log_{10} J(1.4^\circ) = 15.7$ .

Given the present data, we make predictions with the full  $J - L_V$  relation for galaxy candidates without kinematics in Table 2. Comparable predictions with the distance scaling relation can be found in Table 1 of Albert et al. (2017b).

#### 4.8 Limitations

As emphasized above, to obtain the J and D-factors, we have implemented the standard spherical Jeans-based likelihood analysis. We have chosen this method for the simplicity in interpretation of the results, and to perform a fair comparison with previous authors who have performed similar analyses.

We note, however, that there are some limitations to our likelihood model. First we have fixed to the dark matter halo profile to be an NFW profile. Several works have presented generalized dark matter profiles (e.g. Geringer-Sameth et al. 2015b; Bonnivard et al.

**Table 2.** Predictions for galaxies without kinematics based on Equation 12. Citations: (a) (Drlica-Wagner et al. 2015b) (b) (Homma et al. 2017) (c) (Carlin et al. 2017) (d) (Kim & Jerjen 2015) (e) (Drlica-Wagner et al. 2016) (f) (Bechtol et al. 2015) (g) (Laevens et al. 2015b)

Galaxy	$L_V$ $L_\odot$	$r_{1/2}$ pc	$d$ kpc	$J(0.5^\circ)$ $\text{GeV}^2 \text{cm}^{-5}$	Citation
Cetus II	8.6e1	17	30	19.1	a
Cetus III	8.2e2	44	251	17.2	b
Columba I	4.1e3	98	183	17.3	c
Grus II	3.1e3	93	53	18.4	a
Horologium II	94e2	33	78	18.3	d
Indus II	4.5e3	181	214	16.9	a
Pictor II	1.6e3	46	45	18.7	e
Pictoris I	2.6e3	43	126	17.9	f
Phoenix II	26e3	33	95	18.3	f
Reticulum III	1.8e3	64	92	18.0	a
Sagittarius II	1.0e4	33	67	18.7	g
Tucana IV	2.1e3	98	48	18.4	a
Tucana V	3.7e2	9.3	55	19.0	a
Virgo I	1.2e2	30	91	17.9	b

2015b). When allowing for a more flexible model for the dark matter halo, the general trend is toward increasing the J-factor, though there are no substantial biases in the results. A second limitation may be in our parameterization of the stellar velocity anisotropy profile. The APOSTLE hydrodynamical simulations find stellar anisotropy profiles that can be well approximated as constant profiles (Campbell et al. 2017). Chiappo et al. (2017) have studied in particular the different between constant and Osipkov-Merritt anisotropy profiles in J-Factor analysis. Given the small data sets for many of the dSphs we have studied, our assumptions for stellar anisotropy and stellar density profiles are adequate. This is particularly true for ultra-faints, though for the brightest dSphs a more flexible model may be ultimately required.

We have also assumed spherical symmetry for our dynamical models. Deviations from spherical symmetry have been studied in previous J-factors analysis, including the use of axisymmetric Jeans modeling (Hayashi et al. 2016) and made-to-measure models (Sanders et al. 2016). It is also worth noting that incorrect dSph membership can affect the inferred velocity dispersion and therefore J-Factor in ultra-faints (Bonnivard et al. 2016; Ichikawa et al. 2017), though this is less of a problem in the bright classical satellites. We have modified some commonly used spectroscopic data sets, mostly removing RR Lyrae stars (dSph members but the stars are variable in velocity). Binary stars can inflate the velocity dispersion of dSphs and therefore inflate the J-Factors (Minor et al. 2010; McConnachie & Côté 2010; Kirby et al. 2017; Spencer et al. 2017a). If binary stars have inflated the velocity dispersion, than our scaling relations imply that the J and D-Factors will be simply scaled down ( $\sigma_{\text{true}}/\sigma_{\text{inflated}}$ ) $^\alpha$  with  $\alpha = 4, 2$  respectively. Inflated  $\sigma_{\text{los}}$  values could potentially affect the derived normalizations ( $J_0/D_0$ ) for our scaling relations but this requires future multi-epoch data to test.

## 5 CONCLUSION

In this paper we have presented a compilation of J and D-Factors for MW, M31, and LF dSphs. In addition to adding new J and D-factor calculations for newly-discovered MW satellites (Aquarius II and Pegasus III), we provide the first calculations for satel-

lites of M31 and within the local field between the MW and M31. From this compilation, we derive scaling relations for the J and D-Factors. We find a scaling relation for the J-Factor to be:  $J \propto \sigma_{\text{los}}^4/d^2/r_{1/2}$  and find the respective relation for the D-Factor to be:  $D \propto \sigma_{\text{los}}^2 r_{1/2}/d^2$ . The strongest scaling for the J-Factor is based on  $\sigma_{\text{los}}$  or dynamical mass but due to the small relative range of  $\sigma_{\text{los}}$  for the MW satellites ( $\sigma_{\text{los}} \approx 2 - 13 \text{ km s}^{-1}$ ) this scaling is hard to pick out over the distance scaling ( $d \approx 20 - 450 \text{ kpc}$ ). We further find that there is no strong scaling with the stellar luminosity.

While performing a dynamical modeling as outlined in Section 3 is ideal for computing the J and D-Factors, for small data samples and for systems with unresolved velocity dispersions this full analysis may not be feasible. It is in these instances in which the scaling relations are particularly important to provide an estimate of the J and D-factors.

Improved galaxy kinematics in the ultra-low luminosity region is required to ultimately test the scaling relations we have discussed. However, with current observational facilities, it is likely difficult to significantly improve upon the stellar kinematics of known dSphs, especially the faintest-known systems. It would be particularly interesting if a larger data sample reveals a scaling between the luminosity and the J or D-factors. Though the scaling with  $L_V$  does not do better than pure distance scaling given the current data, if more data were to reveal a  $J - L_V$  scaling, such a relation would be especially useful to estimate the J-Factor for galaxies before they are followed up spectroscopically. This will likely be especially true in the LSST era, during which many low luminosity dSphs are predicted to be discovered (e.g. Hargis et al. 2014) and spectroscopic characterization and dark matter properties may be difficult before 30-meter class facilities become available.

## ACKNOWLEDGMENTS

We thank Josh Simon and Matt Walker for providing spectroscopic data. LES acknowledges support from DOE Grant de-sc0010813. We acknowledge generous support from the Texas A&M University and the George P. and Cynthia Woods Institute for Fundamental Physics and Astronomy.

Databases and software: Python packages: `Astropy`<sup>8</sup> (Astropy Collaboration et al. 2013), `NumPy` (Walt et al. 2011), `iPython` (Pérez & Granger 2007), `SciPy` (Jones et al. 2001), `matplotlib` (Hunter 2007), and `corner` (Foreman-Mackey 2016). This research has made use of NASA’s Astrophysics Data System Bibliographic Services.

## REFERENCES

- Abdo A. A., et al., 2010, *ApJ*, 712, 147
- Abramowski A., et al., 2014, *Phys. Rev. D*, 90, 112012
- Ackermann M., et al., 2011, *Physical Review Letters*, 107, 241302
- Ackermann M., et al., 2014, *Phys. Rev. D*, 89, 042001
- Ackermann M., et al., 2015, *Physical Review Letters*, 115, 231301
- Adén D., et al., 2009, *A&A*, 506, 1147
- Albert A., et al., 2017a, preprint, ([arXiv:1706.01277](https://arxiv.org/abs/1706.01277))
- Albert A., et al., 2017b, *ApJ*, 834, 110
- Archambault S., et al., 2017, *Phys. Rev. D*, 95, 082001
- Astropy Collaboration et al., 2013, *A&A*, 558, A33
- Bate N. F., McMonigal B., Lewis G. F., Irwin M. J., Gonzalez-Solares E., Shanks T., Metcalfe N., 2015, *MNRAS*, 453, 690

<sup>8</sup> <http://www.astropy.org>

- Bechtol K., et al., 2015, *ApJ*, **807**, 50
- Bellazzini M., Ferraro F. R., Origlia L., Pancino E., Monaco L., Oliva E., 2002, *AJ*, **124**, 3222
- Bellazzini M., Gennari N., Ferraro F. R., 2005, *MNRAS*, **360**, 185
- Belokurov V., et al., 2007, *ApJ*, **654**, 897
- Belokurov V., et al., 2009, *MNRAS*, **397**, 1748
- Bernard E. J., et al., 2009, *ApJ*, **699**, 1742
- Boettcher E., et al., 2013, *AJ*, **146**, 94
- Bonanos A. Z., Stanek K. Z., Szentgyorgyi A. H., Sasselov D. D., Bakos G. Á., 2004, *AJ*, **127**, 861
- Bonniard V., Combet C., Maurin D., Walker M. G., 2015a, *MNRAS*, **446**, 3002
- Bonniard V., et al., 2015b, *MNRAS*, **453**, 849
- Bonniard V., Maurin D., Walker M. G., 2016, *MNRAS*, **462**, 223
- Caldwell N., et al., 2017, *ApJ*, **839**, 20
- Campbell D. J. R., et al., 2017, *MNRAS*, **469**, 2335
- Carlin J. L., et al., 2017, *AJ*, **154**, 267
- Casetti-Dinescu D. I., Girard T. M., Schriefer M., 2017, preprint, ([arXiv:1710.02462](https://arxiv.org/abs/1710.02462))
- Charbonnier A., et al., 2011, *MNRAS*, **418**, 1526
- Chiappo A., Cohen-Tanugi J., Conrad J., Strigari L. E., Anderson B., Sánchez-Conde M. A., 2017, *MNRAS*, **466**, 669
- Cicuendez L., et al., 2017, preprint, ([arXiv:1709.04519](https://arxiv.org/abs/1709.04519))
- Coleman M. G., Jordi K., Rix H.-W., Grebel E. K., Koch A., 2007a, *AJ*, **134**, 1938
- Coleman M. G., et al., 2007b, *ApJ*, **668**, L43
- Collins M. L. M., et al., 2013, *ApJ*, **768**, 172
- Collins M. L. M., Tollerud E. J., Sand D. J., Bonaca A., Willman B., Strader J., 2017, *MNRAS*, **467**, 573
- Conn A. R., et al., 2012, *ApJ*, **758**, 11
- Conrad J., Cohen-Tanugi J., Strigari L. E., 2015, *Soviet Journal of Experimental and Theoretical Physics*, **121**, 1104
- Crnojević D., Sand D. J., Zaritsky D., Spekkens K., Willman B., Hargis J. R., 2016, *ApJ*, **824**, L14
- Dall'Ora M., et al., 2006, *ApJ*, **653**, L109
- Dall'Ora M., et al., 2012, *ApJ*, **752**, 42
- Deason A. J., Belokurov V., Evans N. W., Watkins L. L., Fellhauer M., 2012, *MNRAS*, **425**, L101
- Drlica-Wagner A., et al., 2015a, *ApJ*, **809**, L4
- Drlica-Wagner A., et al., 2015b, *ApJ*, **813**, 109
- Drlica-Wagner A., et al., 2016, *ApJ*, **833**, L5
- Eadie G. M., Harris W. E., 2016, *ApJ*, **829**, 108
- Evans N. W., Ferrer F., Sarkar S., 2004, *Phys. Rev. D*, **69**, 123501
- Evans N. W., Sanders J. L., Geringer-Sameth A., 2016, *Phys. Rev. D*, **93**, 103512
- Feroz F., Hobson M. P., 2008, *MNRAS*, **384**, 449
- Feroz F., Hobson M. P., Bridges M., 2009, *MNRAS*, **398**, 1601
- Foreman-Mackey D., 2016, *The Journal of Open Source Software*, 24
- Fraternali F., Tolstoy E., Irwin M. J., Cole A. A., 2009, *A&A*, **499**, 121
- Frebel A., Simon J. D., Geha M., Willman B., 2010, *ApJ*, **708**, 560
- Gammaldi V., Karukes E. V., Salucci P., 2017, preprint, ([arXiv:1706.01843](https://arxiv.org/abs/1706.01843))
- Garling C., et al., 2018, *ApJ*, **852**, 44
- Garofalo A., et al., 2013, *ApJ*, **767**, 62
- Garrison-Kimmel S., Boylan-Kolchin M., Bullock J. S., Kirby E. N., 2014, *MNRAS*, **444**, 222
- Geringer-Sameth A., Koushiappas S. M., 2011, *Physical Review Letters*, **107**, 241303
- Geringer-Sameth A., Koushiappas S. M., Walker M. G., 2015a, *Phys. Rev. D*, **91**, 083535
- Geringer-Sameth A., Koushiappas S. M., Walker M., 2015b, *ApJ*, **801**, 74
- Greco C., et al., 2008, *ApJ*, **675**, L73
- Hargis J. R., Willman B., Peter A. H. G., 2014, *ApJ*, **795**, L13
- Hayashi K., Ichikawa K., Matsumoto S., Ibe M., Ishigaki M. N., Sugai H., 2016, *MNRAS*, **461**, 2914
- Homma D., et al., 2017, preprint, ([arXiv:1704.05977](https://arxiv.org/abs/1704.05977))
- Hunter J. D., 2007, *Computing in Science & Engineering*, 9, 90
- Ichikawa K., Horigome S.-i., Ishigaki M. N., Matsumoto S., Ibe M., Sugai H., Hayashi K., 2017, preprint, ([arXiv:1706.05481](https://arxiv.org/abs/1706.05481))
- Irwin M., Hatzidimitriou D., 1995, *MNRAS*, **277**, 1354
- Jones E., Oliphant T., Peterson P., et al., 2001, SciPy: Open source scientific tools for Python, <http://www.scipy.org/>
- Kacharov N., et al., 2017, *MNRAS*, **466**, 2006
- Kaplinghat M., Strigari L. E., 2008, *ApJ*, **682**, L93
- Karczmarek P., et al., 2015, *AJ*, **150**, 90
- Kim D., Jerjen H., 2015, *ApJ*, **808**, L39
- Kim D., et al., 2016, *ApJ*, **833**, 16
- Kirby E. N., Boylan-Kolchin M., Cohen J. G., Geha M., Bullock J. S., Kaplinghat M., 2013, *ApJ*, **770**, 16
- Kirby E. N., Bullock J. S., Boylan-Kolchin M., Kaplinghat M., Cohen J. G., 2014, *MNRAS*, **439**, 1015
- Kirby E. N., Simon J. D., Cohen J. G., 2015, *ApJ*, **810**, 56
- Kirby E. N., Cohen J. G., Simon J. D., Guhathakurta P., Thygesen A. O., Duggan G. E., 2017, *ApJ*, **838**, 83
- Kleyne J. T., Geller M. J., Kenyon S. J., Kurtz M. J., Thorstensen J. R., 1998, *AJ*, **115**, 2359
- Klop N., Zandanel F., Hayashi K., Ando S., 2017, *Phys. Rev. D*, **95**, 123012
- Koch A., Hansen T., Feltzing S., Wilkinson M. I., 2014, *ApJ*, **780**, 91
- Koposov S. E., et al., 2011, *ApJ*, **736**, 146
- Koposov S. E., Belokurov V., Torrealba G., Evans N. W., 2015a, *ApJ*, **805**, 130
- Koposov S. E., et al., 2015b, *ApJ*, **811**, 62
- Kuehn C., et al., 2008, *ApJ*, **674**, L81
- Küpper A. H. W., Johnston K. V., Mieske S., Collins M. L. M., Tollerud E. J., 2017, *ApJ*, **834**, 112
- Laevens B. P. M., et al., 2015a, *ApJ*, **802**, L18
- Laevens B. P. M., et al., 2015b, *ApJ*, **813**, 44
- Li T. S., et al., 2017, *ApJ*, **838**, 8
- MAGIC Collaboration 2016, *J. Cosmology Astropart. Phys.*, **2**, 039
- Martin N. F., de Jong J. T. A., Rix H.-W., 2008, *ApJ*, **684**, 1075
- Martin N. F., et al., 2015, *ApJ*, **804**, L5
- Martin N. F., et al., 2016a, *MNRAS*, **458**, L59
- Martin N. F., et al., 2016b, *ApJ*, **833**, 167
- Martinez G. D., 2015, *MNRAS*, **451**, 2524
- Martínez-Vázquez C. E., et al., 2015, *MNRAS*, **454**, 1509
- Martinez G. D., Bullock J. S., Kaplinghat M., Strigari L. E., Trotta R., 2009, *J. Cosmology Astropart. Phys.*, **6**, 14
- Mateo M., Olszewski E. W., Walker M. G., 2008, *ApJ*, **675**, 201
- McConnachie A. W., 2012, *AJ*, **144**, 4
- McConnachie A. W., Côté P., 2010, *ApJ*, **722**, L209
- McConnachie A. W., Irwin M. J., 2006, *MNRAS*, **365**, 1263
- McConnachie A. W., Irwin M. J., Ferguson A. M. N., Ibata R. A., Lewis G. F., Tanvir N., 2005, *MNRAS*, **356**, 979
- McMonigal B., et al., 2014, *MNRAS*, **444**, 3139
- Medina G. E., et al., 2017, *ApJ*, **845**, L10
- Minor Q. E., Martinez G., Bullock J., Kaplinghat M., Trainor R., 2010, *ApJ*, **721**, 1142
- Moretti M. I., et al., 2009, *ApJ*, **699**, L125
- Muñoz R. R., Geha M., Willman B., 2010, *AJ*, **140**, 138
- Musella I., et al., 2009, *ApJ*, **695**, L83
- Musella I., et al., 2012, *ApJ*, **756**, 121
- Navarro J. F., Frenk C. S., White S. D. M., 1996, *ApJ*, **462**, 563
- Okamoto S., Arimoto N., Yamada Y., Onodera M., 2008, *A&A*, **487**, 103
- Okamoto S., Arimoto N., Yamada Y., Onodera M., 2012, *ApJ*, **744**, 96
- Okamoto S., Arimoto N., Tolstoy E., Jablonka P., Irwin M. J., Komiyama Y., Yamada Y., Onodera M., 2017, *MNRAS*, **467**, 208
- Pérez F., Granger B. E., 2007, *Computing in Science and Engineering*, 9, 21
- Piatek S., Pryor C., Olszewski E. W., Harris H. C., Mateo M., Minniti D., Tinney C. G., 2003, *AJ*, **126**, 2346
- Piatek S., Pryor C., Bristow P., Olszewski E. W., Harris H. C., Mateo M., Minniti D., Tinney C. G., 2005, *AJ*, **130**, 95
- Piatek S., Pryor C., Bristow P., Olszewski E. W., Harris H. C., Mateo M., Minniti D., Tinney C. G., 2007, *AJ*, **133**, 818
- Piatek S., Pryor C., Olszewski E. W., 2016, *AJ*, **152**, 166

- Pietrzyński G., Górska M., Gieren W., Ivanov V. D., Bresolin F., Kudritzki R.-P., 2009, *AJ*, **138**, 459
- Plummer H. C., 1911, *MNRAS*, **71**, 460
- Read J. I., Steger P., 2017, *MNRAS*, **471**, 4541
- Read J. I., Wilkinson M. I., Evans N. W., Gilmore G., Kleyna J. T., 2006, *MNRAS*, **367**, 387
- Sand D. J., Strader J., Willman B., Zaritsky D., McLeod B., Caldwell N., Seth A., Olszewski E., 2012, *ApJ*, **756**, 79
- Sanders J. L., Evans N. W., Geringer-Sameth A., Dehnen W., 2016, *Phys. Rev. D*, **94**, 063521
- Siegel M. H., Shetrone M. D., Irwin M., 2008, *AJ*, **135**, 2084
- Simon J. D., Geha M., 2007, *ApJ*, **670**, 313
- Simon J. D., et al., 2011, *ApJ*, **733**, 46
- Simon J. D., et al., 2015, *ApJ*, **808**, 95
- Simon J. D., et al., 2017, *ApJ*, **838**, 11
- Smolčić V., Zucker D. B., Bell E. F., Coleman M. G., Rix H. W., Schinnerer E., Ivezić Ž., Kniazev A., 2007, *AJ*, **134**, 1901
- Sofue Y., 2015, *PASJ*, **67**, 75
- Sohn S. T., Besla G., van der Marel R. P., Boylan-Kolchin M., Majewski S. R., Bullock J. S., 2013, *ApJ*, **768**, 139
- Sohn S. T., et al., 2017, *ApJ*, **849**, 93
- Spencer M. E., Mateo M., Walker M. G., Olszewski E. W., McConnachie A. W., Kirby E. N., Koch A., 2017a, *AJ*, **153**, 254
- Spencer M. E., Mateo M., Walker M. G., Olszewski E. W., 2017b, *ApJ*, **836**, 202
- Springel V., et al., 2008, *MNRAS*, **391**, 1685
- Stetson P. B., Fiorentino G., Bono G., Bernard E. J., Monelli M., Iannicola G., Gallart C., Ferraro I., 2014, *PASP*, **126**, 616
- Strigari L. E., Koushiappas S. M., Bullock J. S., Kaplinghat M., 2007, *Phys. Rev. D*, **75**, 083526
- Strigari L. E., Bullock J. S., Kaplinghat M., Simon J. D., Geha M., Willman B., Walker M. G., 2008a, *Nature*, **454**, 1096
- Strigari L. E., Koushiappas S. M., Bullock J. S., Kaplinghat M., Simon J. D., Geha M., Willman B., 2008b, *ApJ*, **678**, 614
- Strigari L. E., Frenk C. S., White S. D. M., 2010, *MNRAS*, **408**, 2364
- Tollerud E. J., et al., 2012, *ApJ*, **752**, 45
- Torrealba G., Koposov S. E., Belokurov V., Irwin M., 2016a, *MNRAS*, **459**, 2370
- Torrealba G., et al., 2016b, *MNRAS*, **463**, 712
- Torrealba G., et al., 2018, *MNRAS*,
- Vivas A. K., et al., 2016, *AJ*, **151**, 118
- Walker M. G., Mateo M., Olszewski E. W., Bernstein R., Wang X., Woodroffe M., 2006, *AJ*, **131**, 2114
- Walker M. G., Mateo M., Olszewski E. W., 2008, *ApJ*, **688**, L75
- Walker M. G., Mateo M., Olszewski E. W., 2009a, *AJ*, **137**, 3100
- Walker M. G., Mateo M., Olszewski E. W., Sen B., Woodroffe M., 2009b, *AJ*, **137**, 3109
- Walker M. G., Belokurov V., Evans N. W., Irwin M. J., Mateo M., Olszewski E. W., Gilmore G., 2009c, *ApJ*, **694**, L144
- Walker M. G., Mateo M., Olszewski E. W., Peñarrubia J., Wyn Evans N., Gilmore G., 2009d, *ApJ*, **704**, 1274
- Walker M. G., Combet C., Hinton J. A., Maurin D., Wilkinson M. I., 2011, *ApJ*, **733**, L46
- Walker M. G., Olszewski E. W., Mateo M., 2015, *MNRAS*, **448**, 2717
- Walker M. G., et al., 2016, *ApJ*, **819**, 53
- Walt S. v. d., Colbert S. C., Varoquaux G., 2011, *Computing in Science & Engineering*, **13**, 22
- Willman B., et al., 2005, *AJ*, **129**, 2692
- Willman B., Geha M., Strader J., Strigari L. E., Simon J. D., Kirby E., Ho N., Warres A., 2011, *AJ*, **142**, 128
- Wolf J., Martinez G. D., Bullock J. S., Kaplinghat M., Geha M., Muñoz R. R., Simon J. D., Avedo F. F., 2010, *MNRAS*, **406**, 1220
- de Jong J. T. A., et al., 2008, *ApJ*, **680**, 1112

## APPENDIX A: ANALYTIC DERIVATION OF THE J-FACTOR SCALING RELATION

We begin with the analytic form of the NFW J-Factor (Equation 16 of Evans et al. 2016):

$$J(\theta) = \frac{\pi \rho_s^2 r_s^3}{3d^2} \frac{1}{\Delta^2} \left[ 2y \left( 7y - 4y^3 + 3\pi\Delta^4 \right) + 6 \left( 2\Delta^6 - 2\Delta^2 - y^4 \right) \frac{1}{\Delta} \text{Arcsech}(y) \right]$$

$$J(\theta) = \frac{\pi \rho_s^2 r_s^3}{3d^2} f(d\theta/r_s) \quad (\text{A1})$$

where  $y = d\theta/r_s$  and  $\Delta^2 = 1 - y^2$ . For brevity we will write the functional portion of Equation A1 as  $f(d\theta/r_s)$ . For the NFW mass profile:

$$\rho_s r_s = \frac{M_{1/2}}{4\pi r_s^2 g(r_{1/2}/r_s)} = \frac{5\sigma_{\text{los}}^2 r_{1/2}}{2G} \frac{1}{4\pi r_s^2 g(r_{1/2}/r_s)} \quad (\text{A2})$$

where  $g(x) = \log 1 + x - x/(1 + x)$  and the later equality follows from the half-mass estimators (Walker et al. 2009d; Wolf et al. 2010).

Replacing  $\rho_s$  in Equation A1 with Equation A2 and examining  $\theta = \alpha_c = 2r_{1/2}/d$  we find:

$$J(\alpha_c) = \frac{\pi r_s}{3d^2} \left( \frac{5\sigma_{\text{los}}^2 r_{1/2}}{8\pi G r_s^2} \frac{1}{g(r_{1/2}/r_s)} \right)^2 f(2r_{1/2}/r_s)$$

$$= \frac{25}{192\pi} \frac{\sigma_{\text{los}}^4}{G^2 r_{1/2}^2 d^2} \left( \frac{r_{1/2}}{r_s} \right)^3 \frac{f(2r_{1/2}/r_s)}{\left[ g(r_{1/2}/r_s) \right]^2}$$

$$= \frac{\sigma_{\text{los}}^4}{G^2 r_{1/2}^2 d^2} F(r_{1/2}/r_s)$$

In the last line we have moved all the numerical constants and the  $r_{1/2}/r_s$  dependence into a single function. If we assume  $r_{1/2}/r_s \approx 0.25$ , we find the same normalization as our scaling relation.

Table A1: Errors are  $\pm 1\sigma$  for original study. Photometric properties, spectroscopic source, J and D-factor results for all objects in our study. Description of columns: (1) Name of galaxy. (2) Heliocentric distance ( $d$ ; kpc). (3) Azimuthally averaged half-light radius ( $r_{1/2}$ ; pc). (4) Velocity dispersion ( $\sigma_{\text{los}}$ ;  $\text{km s}^{-1}$ ). (5) Number of spectroscopic members including data source. (6) V-Band absolute magnitude. (7)  $\alpha_c \approx 2r_{1/2}/d$  (degree) (Walker et al. 2011) (8, 9, 10) J-Factor ( $\log_{10}$ ;  $\text{GeV}^2 \text{cm}^{-5}$ ) within angular cone of  $\theta_{\text{max}} = 0.1^\circ, 0.5^\circ, \alpha_c$ . (11, 12, 13) D-Factor ( $\log_{10}$ ;  $\text{GeV cm}^{-2}$ ) within angular cone of  $\theta_{\text{max}} = 0.1^\circ, 0.5^\circ, \alpha_c/2$ . The distance column error bars reflect numbers quoted in the original study and  $r_{1/2}$  error bars include errors on distance, major-axis half-light radius, and ellipticity. For all other values the median value is displayed and error bars refer to the 15.87% and 84.13% confidence intervals. Upper limits are quoted at 99.5% confidence interval. Letters in columns refer to the following citations: (a) (Kuehn et al. 2008) (b) (Martin et al. 2008) (c) (Simon & Geha 2007) (d) (Karczmarek et al. 2015) (e) (Irwin & Hatzidimitriou 1995) (f) (Walker et al. 2009a) (g) (McMonigal et al. 2014) (h) (McConnachie 2012) (i) (Bonanos et al. 2004) (j) (Walker et al. 2015) (k) (Pietrzyński et al. 2009) (l) (Bate et al. 2015) (m) (Stetson et al. 2014) (n) (Smolčić et al. 2007) (o) (Mateo et al. 2008) (p) (Bellazzini et al. 2005) (q) (Coleman et al. 2007a) (r) (Spencer et al. 2017b) (s) (Martínez-Vázquez et al. 2015) (t) (Okamoto et al. 2017) (u) (Cicuende et al. 2017) (v) (Bellazzini et al. 2002) (w) (Kleyna et al. 1998) (x) M. Spencer et al., in prep (y) (Torrealba et al. 2016b) (z) (Dall’Ora et al. 2006) (aa) (Koposov et al. 2011) (ab) (Greco et al. 2008) (ac) (Sand et al. 2012) (ad) (Torrealba et al. 2018) (ae) T. S. Li et al., in prep (af) (Musella et al. 2009) (ag) (Muñoz et al. 2010) (ah) (Laevens et al. 2015b) (ai) (Martin et al. 2016a) (aj) (Koposov et al. 2015a) (ak) (Walker et al. 2016) (al) (Musella et al. 2012) (am) (Coleman et al. 2007b) (an) (Bechtol et al. 2015) (ao) (Koposov et al. 2015b) (ap) (Vivas et al. 2016) (aq) (Martin et al. 2015) (ar) (Kirby et al. 2015) (as) (Moretti et al. 2009) (at) (Okamoto et al. 2012) (au) (Medina et al. 2017) (av) (Collins et al. 2017) (aw) (Kim et al. 2016) (ax) (Simon et al. 2015) (ay) (Belokurov et al. 2007) (az) (Simon et al. 2011) (ba) (Boettcher et al. 2013) (bb) (Belokurov et al. 2009) (bc) (Kirby et al. 2013) (bd) (Laevens et al. 2015a) (be) (Kirby et al. 2017) (bf) (Drlica-Wagner et al. 2015b) (bg) (Simon et al. 2017) (bh) (Garofalo et al. 2013) (bi) (Okamoto et al. 2008) (bj) (Dall’Ora et al. 2012) (bk) (Willman et al. 2005) (bl) (Willman et al. 2011) (bm) (Bernard et al. 2009) (bn) (McConnachie & Irwin 2006) (bo) (Kirby et al. 2014) (bp) (Crnojević et al. 2016) (bq) (Li et al. 2017) (br) (de Jong et al. 2008) (bs) (Conn et al. 2012) (bt) (Martin et al. 2016b) (bu) (Tollerud et al. 2012) (bv) (McConnachie et al. 2005)

Galaxy	Distance	$r_{1/2}$	$\sigma$	N	$M_V$	$\alpha_c$	J( $0.1^\circ$ )	J( $0.5^\circ$ )	J( $\alpha_c$ )	D( $0.1^\circ$ )	D( $0.5^\circ$ )	D( $\alpha_c/2$ )
	kpc	pc	$\text{km s}^{-1}$			deg	$\text{GeV}^2 \text{cm}^{-5}$	$\text{GeV}^2 \text{cm}^{-5}$	$\text{GeV}^2 \text{cm}^{-5}$	$\text{GeV cm}^{-2}$	$\text{GeV cm}^{-2}$	$\text{GeV cm}^{-2}$
Canes Venatici I	$210 \pm 6$ (a)	$424 \pm 25$ (b)	$7.6_{-0.4}^{+0.5}$	209(c)	$-8.6 \pm 0.15$	0.232	$17.16_{-0.18}^{+0.19}$	$17.42_{-0.15}^{+0.17}$	$17.33_{-0.15}^{+0.15}$	$16.88_{-0.09}^{+0.11}$	$17.79_{-0.27}^{+0.26}$	$16.98_{-0.10}^{+0.12}$
Carina	$105.6 \pm 5.4$ (d)	$203 \pm 22$ (e)	$6.4_{-0.2}^{+0.2}$	758(f)	$-9.1 \pm 0.4$	0.221	$17.66_{-0.15}^{+0.16}$	$17.91_{-0.09}^{+0.10}$	$17.82_{-0.11}^{+0.12}$	$16.99_{-0.04}^{+0.05}$	$17.87_{-0.15}^{+0.16}$	$17.05_{-0.05}^{+0.05}$
Draco	$76 \pm 6$ (i)	$182 \pm 13$ (b)	$9.1_{-0.3}^{+0.3}$	476(j)	$-8.75 \pm 0.15$	0.276	$18.35_{-0.11}^{+0.14}$	$18.83_{-0.10}^{+0.10}$	$18.68_{-0.10}^{+0.10}$	$17.42_{-0.05}^{+0.06}$	$18.54_{-0.14}^{+0.11}$	$17.66_{-0.06}^{+0.06}$
Fornax	$147 \pm 9$ (k)	$609 \pm 38$ (l)	$10.6_{-0.2}^{+0.2}$	2409(f)	$-13.4 \pm 0.3$	0.476	$17.90_{-0.14}^{+0.12}$	$18.07_{-0.10}^{+0.11}$	$18.07_{-0.10}^{+0.11}$	$17.13_{-0.03}^{+0.04}$	$17.97_{-0.04}^{+0.05}$	$17.62_{-0.03}^{+0.03}$
Leo I	$258.2 \pm 9.5$ (m)	$292 \pm 26$ (n)	$9.0_{-0.4}^{+0.4}$	327(o)	$-12.0 \pm 0.3$	0.13	$17.36_{-0.11}^{+0.12}$	$17.65_{-0.12}^{+0.13}$	$17.43_{-0.10}^{+0.11}$	$17.06_{-0.09}^{+0.09}$	$18.01_{-0.28}^{+0.20}$	$16.76_{-0.07}^{+0.07}$
Leo II	$233 \pm 15$ (p)	$159 \pm 14$ (q)	$7.4_{-0.4}^{+0.4}$	175(r)	$-9.9 \pm 0.3$	0.078	$17.63_{-0.17}^{+0.19}$	$17.76_{-0.17}^{+0.22}$	$17.59_{-0.18}^{+0.20}$	$16.98_{-0.17}^{+0.20}$	$17.65_{-0.35}^{+0.48}$	$16.43_{-0.09}^{+0.11}$
Sculptor	$83.9 \pm 1.5$ (s)	$230 \pm 36$ (e)	$8.8_{-0.2}^{+0.2}$	1349(f)	$-11.04 \pm 0.5$	0.314	$18.30_{-0.14}^{+0.14}$	$18.57_{-0.07}^{+0.08}$	$18.52_{-0.09}^{+0.09}$	$17.28_{-0.03}^{+0.03}$	$18.20_{-0.08}^{+0.09}$	$17.57_{-0.03}^{+0.04}$
Sextans	$92.5 \pm 2.2$ (t)	$524 \pm 23$ (u)	$7.1_{-0.3}^{+0.3}$	424(f)	$-9.1 \pm 0.1$	0.659	$17.37_{-0.24}^{+0.24}$	$17.73_{-0.12}^{+0.13}$	$17.76_{-0.10}^{+0.11}$	$16.90_{-0.05}^{+0.05}$	$17.90_{-0.09}^{+0.11}$	$17.65_{-0.06}^{+0.07}$
Ursa Minor	$76 \pm 4$ (v)	$201 \pm 23$ (w)	$9.3_{-0.4}^{+0.4}$	311(x)	$-8.8 \pm 0.5$	0.305	$18.76_{-0.20}^{+0.16}$	$18.89_{-0.12}^{+0.12}$	$18.87_{-0.14}^{+0.13}$	$17.38_{-0.04}^{+0.04}$	$18.15_{-0.08}^{+0.12}$	$17.61_{-0.05}^{+0.05}$
Aquarius II	$107.9 \pm 3.3$ (y)	$123 \pm 22$ (y)	$6.2_{-1.7}^{+2.6}$	9(y)	$-4.36 \pm 0.14$	0.131	$18.00_{-0.59}^{+0.63}$	$18.27_{-0.59}^{+0.65}$	$18.06_{-0.58}^{+0.63}$	$17.16_{-0.32}^{+0.35}$	$18.07_{-0.50}^{+0.48}$	$16.88_{-0.31}^{+0.34}$
Bootes I	$66 \pm 3$ (z)	$187 \pm 20$ (b)	$4.9_{-0.6}^{+0.7}$	37(aa)	$-6.3 \pm 0.2$	0.325	$17.76_{-0.28}^{+0.29}$	$18.16_{-0.28}^{+0.30}$	$18.08_{-0.27}^{+0.28}$	$17.04_{-0.15}^{+0.17}$	$18.10_{-0.30}^{+0.25}$	$17.38_{-0.17}^{+0.19}$
Canes Venatici II	$160 \pm 7$ (ab)	$68 \pm 8$ (ac)	$4.7_{-1.0}^{+1.2}$	25(c)	$-4.6 \pm 0.2$	0.049	$17.52_{-0.41}^{+0.42}$	$17.82_{-0.46}^{+0.46}$	$17.32_{-0.41}^{+0.42}$	$17.04_{-0.29}^{+0.26}$	$18.01_{-0.53}^{+0.35}$	$16.05_{-0.22}^{+0.22}$
Carina II	$37.4 \pm 0.4$ (ad)	$76 \pm 8$ (ad)	$3.4_{-0.8}^{+1.2}$	14(ae)	$-4.4 \pm 0.1$	0.234	$17.86_{-0.53}^{+0.56}$	$18.24_{-0.53}^{+0.53}$	$18.09_{-0.52}^{+0.54}$	$16.95_{-0.28}^{+0.29}$	$17.95_{-0.40}^{+0.38}$	$17.06_{-0.28}^{+0.29}$
Coma Berenices	$42 \pm 1.5$ (af)	$57 \pm 4$ (ag)	$4.7_{-0.8}^{+0.9}$	58(c)	$-3.9 \pm 0.6$	0.157	$18.59_{-0.32}^{+0.31}$	$19.00_{-0.36}^{+0.35}$	$18.73_{-0.32}^{+0.31}$	$17.37_{-0.21}^{+0.21}$	$18.45_{-0.43}^{+0.30}$	$17.20_{-0.20}^{+0.20}$
Draco II*	$20.0 \pm 3.0$ (ah)	$12 \pm 5$ (ah)	$3.4_{-1.9}^{+2.5}$	9(ai)	$-2.9 \pm 0.8$	0.071	$18.60_{-1.65}^{+1.29}$	$18.97_{-1.69}^{+1.29}$	$18.51_{-1.67}^{+1.29}$	$17.13_{-0.87}^{+0.68}$	$18.04_{-0.88}^{+0.85}$	$16.43_{-0.85}^{+0.66}$
Grus I*	$120.2 \pm 11.1$ (aj)	$52 \pm 25$ (aj)	$4.5_{-2.8}^{+5.0}$	5(ak)	$-3.4 \pm 0.3$	0.05	$16.64_{-1.68}^{+1.50}$	$16.87_{-1.68}^{+1.52}$	$16.48_{-1.68}^{+1.50}$	$16.39_{-0.83}^{+0.82}$	$17.20_{-0.91}^{+0.95}$	$15.53_{-0.85}^{+0.75}$
Hercules	$132 \pm 6$ (al)	$106 \pm 13$ (am)	$3.9_{-1.0}^{+1.3}$	30(c)	$-6.6 \pm 0.3$	0.092	$17.11_{-0.51}^{+0.51}$	$17.33_{-0.52}^{+0.52}$	$17.09_{-0.51}^{+0.52}$	$16.69_{-0.29}^{+0.29}$	$17.51_{-0.49}^{+0.49}$	$16.21_{-0.26}^{+0.26}$
Horologium I	$87 \pm 8$ (an)	$32 \pm 5$ (an)	$5.9_{-1.8}^{+3.3}$	5(ao)	$-3.5 \pm 0.3$	0.047	$19.00_{-0.63}^{+0.76}$	$19.25_{-0.70}^{+0.79}$	$18.82_{-0.63}^{+0.76}$	$17.53_{-0.46}^{+0.44}$	$18.38_{-0.77}^{+0.63}$	$16.58_{-0.34}^{+0.39}$
Horologium I	$79 \pm 7$ (aj)	$60 \pm 35$ (aj)	$5.9_{-1.8}^{+3.3}$	5(ao)	$-3.4 \pm 0.1$	0.079	$18.59_{-0.78}^{+0.86}$	$18.84_{-0.80}^{+0.89}$	$18.54_{-0.78}^{+0.87}$	$17.34_{-0.45}^{+0.48}$	$18.20_{-0.67}^{+0.65}$	$16.75_{-0.39}^{+0.44}$
Hydra II	$151 \pm 8$ (ap)	$71 \pm 11$ (aq)	$< 6.82$	13(ar)	$-5.1 \pm 0.3$	0.054	$< 17.51$	$< 17.71$	$< 17.37$	$< 16.91$	$< 17.56$	$< 16.02$
Leo IV*	$154 \pm 5$ (as)	$111 \pm 36$ (at)	$3.4_{-1.8}^{+2.0}$	17(c)	$-4.92 \pm 0.2$	0.083	$16.28_{-1.18}^{+0.94}$	$16.50_{-1.16}^{+0.95}$	$16.24_{-1.18}^{+0.95}$	$16.29_{-0.58}^{+0.51}$	$17.08_{-0.62}^{+0.66}$	$15.76_{-0.60}^{+0.47}$
Leo V*	$173 \pm 5$ (au)	$30 \pm 16$ (ac)	$4.9_{-1.9}^{+3.0}$	8(av)	$-4.1 \pm 0.4$	0.02	$17.53_{-0.96}^{+0.89}$	$17.69_{-0.99}^{+0.93}$	$17.19_{-0.98}^{+0.89}$	$16.78_{-0.62}^{+0.57}$	$17.46_{-0.85}^{+0.85}$	$15.38_{-0.48}^{+0.44}$
Pegasus III*	$215 \pm 12$ (aw)	$37 \pm 14$ (aw)	$7.9_{-3.1}^{+4.4}$	7(aw)	$-3.4 \pm 0.4$	0.02	$18.25_{-0.99}^{+0.84}$	$18.41_{-1.04}^{+0.89}$	$17.86_{-0.94}^{+0.82}$	$17.22_{-0.67}^{+0.56}$	$17.93_{-0.90}^{+0.80}$	$15.79_{-0.50}^{+0.42}$

Pisces II*	$183 \pm 15$ (ac)	$48 \pm 10$ (ac)	$4.8^{+3.3}_{-2.0}$	7(ar)	$-4.1 \pm 0.4$	0.03	$17.15^{+0.95}_{-1.08}$	$17.31^{+0.97}_{-1.07}$	$16.92^{+0.98}_{-1.10}$	$16.62^{+0.57}_{-0.57}$	$17.30^{+0.79}_{-0.74}$	$15.50^{+0.47}_{-0.53}$
Reticulum II	$32 \pm 2$ (an)	$34 \pm 8$ (an)	$3.4^{+0.7}_{-0.6}$	25(ax)	$-3.6 \pm 0.1$	0.121	$18.47^{+0.36}_{-0.34}$	$18.87^{+0.39}_{-0.37}$	$18.53^{+0.36}_{-0.33}$	$17.24^{+0.23}_{-0.23}$	$18.30^{+0.33}_{-0.48}$	$16.88^{+0.21}_{-0.20}$
Reticulum II	$30 \pm 2$ (aj)	$32 \pm 3$ (aj)	$3.4^{+0.7}_{-0.6}$	25(ax)	$-2.7 \pm 0.1$	0.121	$18.55^{+0.35}_{-0.33}$	$18.95^{+0.38}_{-0.36}$	$18.60^{+0.34}_{-0.32}$	$17.27^{+0.22}_{-0.23}$	$18.34^{+0.32}_{-0.49}$	$16.91^{+0.20}_{-0.20}$
Segue 1	$23 \pm 2$ (ay)	$21 \pm 5$ (b)	$3.1^{+0.9}_{-0.8}$	62(az)	$-1.5 \pm 0.7$	0.103	$18.85^{+0.55}_{-0.60}$	$19.14^{+0.52}_{-0.59}$	$18.86^{+0.55}_{-0.59}$	$17.23^{+0.29}_{-0.32}$	$18.07^{+0.56}_{-0.49}$	$16.81^{+0.26}_{-0.30}$
Segue 2	$36.6 \pm 2.45$ (ba)	$33 \pm 3$ (bb)	$< 3.20$	25(bc)	$-2.6 \pm 0.1$	0.103	$< 17.84$	$< 18.17$	$< 17.84$	$< 16.86$	$< 17.95$	$< 16.41$
Triangulum II	$30 \pm 2$ (bd)	$28 \pm 8$ (bd)	$< 6.36$	13(be)	$-1.8 \pm 0.5$	0.109	$< 19.36$	$< 19.72$	$< 19.39$	$< 17.62$	$< 18.71$	$< 17.19$
Tucana II	$57.5 \pm 5.3$ (aj)	$162 \pm 35$ (aj)	$7.3^{+2.6}_{-1.7}$	10(ak)	$-3.8 \pm 0.1$	0.325	$18.42^{+0.57}_{-0.50}$	$18.84^{+0.55}_{-0.49}$	$18.75^{+0.55}_{-0.49}$	$17.36^{+0.28}_{-0.25}$	$18.42^{+0.33}_{-0.33}$	$17.69^{+0.29}_{-0.26}$
Tucana II	$57.5 \pm 5.3$ (an)	$115 \pm 32$ (an)	$7.3^{+2.6}_{-1.7}$	10(ak)	$-3.9 \pm 0.2$	0.232	$18.64^{+0.60}_{-0.55}$	$19.02^{+0.57}_{-0.52}$	$18.87^{+0.58}_{-0.53}$	$17.44^{+0.28}_{-0.26}$	$18.46^{+0.35}_{-0.35}$	$17.54^{+0.28}_{-0.27}$
Tucana III	$25 \pm 2$ (bf)	$43 \pm 6$ (bf)	$< 2.18$	26(bg)	$-2.4 \pm 0.2$	0.2	$< 17.31$	$< 17.68$	$< 17.48$	$< 16.56$	$< 17.65$	$< 16.56$
Ursa Major I	$97.3 \pm 5.85$ (bh)	$200 \pm 21$ (bi)	$7.3^{+1.2}_{-1.0}$	36(c)	$-5.5 \pm 0.3$	0.236	$17.94^{+0.34}_{-0.32}$	$18.25^{+0.30}_{-0.28}$	$18.13^{+0.30}_{-0.28}$	$17.15^{+0.16}_{-0.14}$	$18.10^{+0.29}_{-0.29}$	$17.26^{+0.16}_{-0.15}$
Ursa Major II	$34.7 \pm 2.1$ (bj)	$99 \pm 7$ (ag)	$7.2^{+1.8}_{-1.4}$	19(c)	$-4.2 \pm 0.5$	0.327	$18.99^{+0.45}_{-0.41}$	$19.44^{+0.43}_{-0.40}$	$19.34^{+0.43}_{-0.40}$	$17.56^{+0.22}_{-0.21}$	$18.64^{+0.28}_{-0.31}$	$17.91^{+0.23}_{-0.22}$
Willman 1	$38 \pm 7$ (bk)	$18 \pm 4$ (b)	$4.5^{+1.0}_{-0.8}$	40(bl)	$-2.7 \pm 0.7$	0.056	$19.18^{+0.47}_{-0.44}$	$19.51^{+0.49}_{-0.49}$	$19.01^{+0.49}_{-0.44}$	$17.55^{+0.28}_{-0.32}$	$18.52^{+0.46}_{-0.66}$	$16.68^{+0.23}_{-0.22}$
Cetus	$780 \pm 40$ (bm)	$497 \pm 37$ (bn)	$8.2^{+0.8}_{-0.7}$	116(bo)	$-10.1 \pm 0.0$	0.073	$16.20^{+0.21}_{-0.19}$	$16.28^{+0.20}_{-0.19}$	$16.17^{+0.17}_{-0.20}$	$16.45^{+0.17}_{-0.14}$	$17.03^{+0.39}_{-0.26}$	$15.91^{+0.10}_{-0.09}$
Eridanus II	$366 \pm 17$ (bp)	$176 \pm 14$ (bp)	$7.1^{+1.2}_{-0.9}$	28(bq)	$-7.1 \pm 0.3$	0.055	$17.14^{+0.29}_{-0.26}$	$17.29^{+0.35}_{-0.31}$	$17.03^{+0.29}_{-0.26}$	$16.86^{+0.25}_{-0.29}$	$17.60^{+0.48}_{-0.53}$	$16.06^{+0.16}_{-0.15}$
Leo T	$407 \pm 38$ (br)	$142 \pm 36$ (b)	$7.9^{+2.0}_{-1.5}$	19(c)	$-7.1 \pm 0.0$	0.04	$17.35^{+0.45}_{-0.42}$	$17.49^{+0.49}_{-0.46}$	$17.17^{+0.44}_{-0.42}$	$16.94^{+0.33}_{-0.34}$	$17.65^{+0.55}_{-0.58}$	$15.97^{+0.22}_{-0.21}$
And I	$727 \pm 17.5$ (bs)	$699 \pm 29$ (bt)	$10.9^{+2.3}_{-1.7}$	51(bu)	$-11.2 \pm 0.2$	0.11	$16.68^{+0.37}_{-0.36}$	$16.81^{+0.39}_{-0.36}$	$16.69^{+0.37}_{-0.35}$	$16.79^{+0.23}_{-0.21}$	$17.51^{+0.35}_{-0.38}$	$16.43^{+0.21}_{-0.19}$
And III	$723 \pm 21$ (bs)	$296 \pm 33$ (bt)	$9.8^{+1.5}_{-1.3}$	62(bu)	$-9.5 \pm 0.3$	0.047	$16.85^{+0.29}_{-0.27}$	$16.95^{+0.34}_{-0.30}$	$16.73^{+0.30}_{-0.28}$	$16.81^{+0.25}_{-0.29}$	$17.48^{+0.44}_{-0.54}$	$15.94^{+0.16}_{-0.14}$
And V	$742 \pm 21.5$ (bs)	$294 \pm 33$ (bt)	$11.0^{+1.2}_{-1.0}$	85(bu)	$-9.3 \pm 0.2$	0.045	$17.11^{+0.23}_{-0.21}$	$17.19^{+0.29}_{-0.24}$	$16.99^{+0.23}_{-0.21}$	$16.92^{+0.26}_{-0.29}$	$17.55^{+0.49}_{-0.51}$	$16.04^{+0.13}_{-0.12}$
And VII	$763 \pm 35$ (bv)	$717 \pm 39$ (bn)	$13.3^{+1.0}_{-1.0}$	136(bu)	$-12.2 \pm 0.0$	0.108	$16.89^{+0.17}_{-0.17}$	$16.98^{+0.16}_{-0.15}$	$16.90^{+0.17}_{-0.16}$	$16.84^{+0.13}_{-0.11}$	$17.46^{+0.34}_{-0.21}$	$16.50^{+0.09}_{-0.08}$
And XIV	$793 \pm 50$ (bs)	$297 \pm 53$ (bt)	$5.9^{+1.0}_{-0.9}$	48(bu)	$-8.5 \pm 0.35$	0.043	$15.65^{+0.37}_{-0.38}$	$15.74^{+0.39}_{-0.39}$	$15.52^{+0.39}_{-0.38}$	$16.18^{+0.28}_{-0.29}$	$16.78^{+0.48}_{-0.51}$	$15.29^{+0.19}_{-0.19}$
And XVIII	$1214 \pm 41.5$ (bs)	$260 \pm 38$ (bt)	$10.5^{+2.8}_{-2.1}$	22(bu)	$-9.2 \pm 0.35$	0.025	$16.70^{+0.46}_{-0.43}$	$16.76^{+0.47}_{-0.45}$	$16.53^{+0.45}_{-0.43}$	$16.68^{+0.39}_{-0.41}$	$17.21^{+0.59}_{-0.58}$	$15.54^{+0.23}_{-0.22}$

\* Galaxy contains tail in posterior ( $\sigma_{\text{los}}$  and  $J/D$ ) distributions. Values should be used with caution.

This paper has been typeset from a  $\text{\TeX}/\text{\LaTeX}$  file prepared by the author.